Energy 309 (2024) 133123

Contents lists available at ScienceDirect

Energy

journal homepage: www.elsevier.com/locate/energy

Enhancing the efficiency of Brown 24 pigment production through continuous microwave heating in conveyor belt and rotary kiln systems: A design and optimization study

Pedro A.V. Ramos [a,*], Duarte M.S. Albuquerque [a,b,c], José C.F. Pereira [a]

[a] IDMEC, Instituto Superior Técnico, Universidade de Lisboa, Av. Rovisco Pais 1, 1049-001 Lisboa, Portugal
[b] UNIDEMI, Department of Mechanical and Industrial Engineering, NOVA School of Science and Technology, Universidade NOVA de Lisboa, 2829-516, Caparica, Portugal
[c] Laboratório Associado de Sistemas Inteligentes (LASI), 4800-058, Guimarães, Portugal

ARTICLE INFO

Keywords:
Energy efficiency
Integrated energy system
Numerical simulation and optimization
Ceramic pigments
High temperature continuous microwave heating
Automatic impedance matching

ABSTRACT

In energy intensive industries, the continuous production with microwave technology presents several challenges in achieving high energy efficiency and heating uniformity. In the ceramic pigments sector, the Brown 24 is the ideal candidate for this study due to its susceptibility to thermal runaways and its high temperature to reach total conversion, higher than 1000 K. By another hand, most literature related to this field focus on static systems while ignoring the continuous ones which are required by the industry.

A coupled model that integrates thermal, electromagnetic and chemical phenomena within an energy system was implemented in *COMSOL Multiphysics*. Additionally, a MATLAB controller was employed to dynamically adjust the cavity length through a moving plunger, which maximizes the electrical efficiency. The required power is also managed to guarantee a total chemical conversion of the material. The proposed optimization methodology reduces computational costs, and it is applicable to any continuous microwave system processing moving solid materials.

In this work, two microwave configurations were optimized. The first one, based on a conveyor belt, achieved a global efficiency close to 70%. While the second one, based on a rotary kiln, achieved a global efficiency of 85% and a production rate of 4.66 kg/h, significantly outperforming a previous study by factors of 1.57 and 2.06, respectively. These findings show the potential for substantial improvements in continuous microwave systems.

1. Introduction

According to the results published by the Intergovernmental Panel on Climate Change (IPCC) [1], in order to limit the increase (relatively to the pre-industrial era) in the global surface temperature to 1.5 °C in 2100, the green-house gases (GHG) emission balance must be null in 2050 and negative from 2050 to 2100, with an increasing deficit in this period [1]. As such, there is an urgent need to replace traditional heating via fossil fuels, which are responsible for significant amounts of GHG emitted to the atmosphere, causing severe global warming.

The electrification of the industry sector could help to reduce the release of both GHG emissions and pollutants, contributing to the health improvement and economic growth. To achieve these goals, more sustainable heating mechanisms will have to be adopted. Microwave technology may play an important role in this aspect as it combines the high temperature processing of materials with the electricity as the energy source, contributing to the decarbonization process if renewable sources of energy are used to produce the electricity.

Microwave heating results from the interaction between the electromagnetic field and the material. When the electric field changes rapidly, the polarized particles tend to rotate and permanently reorientate in order to align with the field [2]. During this process, energy is dissipated through heat. Thus, microwave heating is highly volumetric if the electric field penetrates sufficiently in the load, which is one of its greatest advantages [3]. Contrarily, in a conventional heating system, the load heats up through convection from the outside to the inside, resulting in high heating times and low efficiencies. As such, microwave heating is rapid, efficient and contributes to a better product quality since the thermal gradients may be reduced if the

* Corresponding author.
E-mail addresses: pedro.v.ramos@tecnico.ulisboa.pt (P.A.V. Ramos), duartealbuquerque@tecnico.ulisboa.pt (D.M.S. Albuquerque), jcfpereira@tecnico.ulisboa.pt (J.C.F. Pereira).

https://doi.org/10.1016/j.energy.2024.133123
Received 27 January 2024; Received in revised form 22 June 2024; Accepted 6 September 2024
Available online 12 September 2024

Nomenclature

Physical constants

ϵ_0	Vacuum dielectric permittivity, $\epsilon_0 = 8.854\times 10^{-12}$ F/m
μ_0	Vacuum magnetic permeability, $\epsilon_0 = 4\pi \times 10^{-7}$ H/m
σ	Stefan–Boltzmann constant, $\sigma = 5.67 \times 10^{-8}$ W/(m^2, K^4)
c_0	Speed of light in vacuum, $c_0 = 3 \times 10^8$ m/s
g	Gravity acceleration, $g = 9.81$ m/s^2
j	Imaginary unit, $j = \sqrt{-1}$
R	Perfect gas constant, $R = 8.314$ J/(mol K)

Greek symbols

α	Conversion degree [–], absorptivity [–]
ΔH	Enthalpy of reaction [J/kg]
δ	Penetration depth [m], loss angle [rad]
ϵ	Electric permittivity [F/m], emissivity [–]
ϵ'	Real part of the electric permittivity [F/m]
ϵ''	Imaginary part of the electric permittivity [F/m]
η_G	Global efficiency [–]
η_M	Magnetron efficiency [–]
η_T	Thermal efficiency [–]
η_{EM}	Electromagnetic efficiency [–]
Γ	Filling angle [rad]
μ	Electric permeability [H/m]
ω	Angular frequency [s^{-1}]
ρ	Density [kg/m^3], reflectivity [–]
ρ_c	Electric charge density [C/m^3]
σ	Electric conductivity [S/m], standard deviation

Roman symbols

A	Area [m^2]
$\mathbf{B}$	Magnetic flux density [Wb/m^2]
b	Bed height [m]
C_e	Specific energy consumption [J/kg]
C_p	Specific heat at constant pressure [J/(kg K)]
$\mathbf{D}$	Electric flux density [C/m^2]
d	Cavity height [m]
D_i	Tube internal diameter [m]
ds	Microwave growth rate [–]
$\mathbf{E}$	Electric field [V/m]
E_a	Activation energy [J/mol]
$e_b(T)$	Black-body emissive power [W/m^2]
$E_{CO_2,eq}$	Specific GHG emissions [$kg_{CO_2,eq}/kg_{pigment}$]
F	View factor [–]
f	Frequency [s^{-1}]
$f(\alpha)$	Kinetic model [–]
f_{GHG}	Conversion factor from electricity [$kg_{CO_2,eq}$/MJ]
G	Irradiation [W/m^2]
$\mathbf{H}$	Magnetic field [A/m]
h	Convection coefficient [W/(m^2 K)]
$\mathbf{J}$	Electric current density [A/m^2]
J	Radiosity [W/m^2]
k	Reaction constant [s^{-1}]; thermal conductivity [W/(m K)]
k_0	Pre-exponential factor [s^{-1}], vacuum wavenumber [m^{-1}]
L	Tube length [m]
$\dot{m}$	Mass flow rate [kg/s]
$\hat{\mathbf{n}}$	Exterior normal unit vector [–]
n	Avrami exponent [–], refractive index [–]
P	Power [W], perimeter [m]
$\dot{Q}$	Heat source [W]
$\dot{Q}_{EM}$	Electromagnetic heat source [W]
$\dot{Q}'''_{EM}$	Electromagnetic heat source per unit volume [W/m^3]
$\dot{\mathbf{q}}''$	Heat flux per unit area [W/m^2]
R	Reaction rate [kg/(m^3 s)]
r	Tube radius [m]
S_{11}	Scattering parameter [–]
T	Temperature [K]
t	Time [s]
T_{ext}	Exterior temperature [K]
$\mathbf{v}$	Axial bed velocity [m/s]
V	Volume [m^3]

Subscripts

adm	Admissible
amb	Ambient
b	Black-body
$conv$	Convection
int	Interpolated
m	Mutual
max	Maximum
min	Minimum
opt	Optimum
r	Relative
rad	Radiation
s	Surface
sim	Simulated

heating is volumetric. Nevertheless, the high heating rates may lead to hot-spots and to the thermal run-away phenomenon [4], specially if the loss tangent increases with temperature and if no temperature control techniques are employed [5]. The study and prediction of these temperature related problems is highly recommended in the Literature, as a safety procedure [6].

Microwave heating was extensively studied in the past few years. Amini et al. [7] perform an extensive research regarding the interaction of microwaves with different types of materials, including metals, metal oxides and susceptors like graphite. The authors report reductions in the energy consumption in the order of 80%, while CO_2 emissions decrease by 75%. Moreover, the numerical simulation is referred to as an important tool that should be employed together with laboratory and large scale experiments to decrease the costs related to the design and the process intensification of microwave reactors.

Several authors have modelled microwave heating devices, being the main contributions summarized in Table 1. Zhu et al. [8] investigated the continuous microwave heating of three different food liquids. The results show that there is a diameter for which the heating efficiency is maximum, being highly dependent on the dielectric properties of the load. Patil et al. [9] studied the microwave heating

Table 1
Summary of the main contributions in the field of microwave heating.

Ref.	Material	Microwave heating	Impedance matching	Design variables	Maximum efficiency [%]	Comments
[8]	Food liquids	Yes	No	Tube diameter and position, cavity shape	99.8	• The optimal solution is highly dependent on the dielectric properties and the maximum efficiency was attained for the configuration where the tube is in the centre of the cavity.
[9]	Ethylene glycol	Yes	Yes, via moving plunger	Tube diameter and position	78%	• For the continuous flow case, the heating efficiency increased monotonously, reaching a maximum for a diameter equal to half wavelength of the electromagnetic field.
[10]	Water	Yes	No	Inlet velocity and tube diameter	62%	• If the dielectric properties are assumed constant, the absorbed power remains practically unchanged for all velocities, which justifies the inclusion of temperature dependent dielectric properties.
[11]	Food liquids	Yes	No	Flow rate	95%	• The numerical results show a good agreement with the experimental data measured by the authors; • The differences were attributed to frequency fluctuations that occurred due to the increase of the magnetron temperature.
[12][1]	Water	Yes	No	Port and tube locations, cavity shape	–	• The load position is one of the studied parameters, showing that the position that guarantees the maximum efficiency is not in the centre of the cavity.
[13]	Ceramic composites	Yes	Yes	Cavity dimensions	60%	• *COMSOL Multiphysics* is used as a design tool to predict the efficiency, the thermal history and the electromagnetic field distribution during the heating inside the cavity.

[1] This reference does not contain the required information to estimate the global efficiency and thus a value is not available.

of ethylene glycol under stationary and continuous flow conditions. An auto tuner was used to maintain the peak of the electric field inside the load and the thermal losses were computed using natural convection correlations, being around 30% of the absorbed power. Yousefi et al. [10] conducted a similar study regarding the microwave heating of water. The diameter that guarantees the maximum electromagnetic efficiency is about 40.5 mm and the reduction of the microwave efficiency for diameters above that value is attributed to the cut-off phenomenon. Tuta and Palazoğlu [11] conducted both numerical and experimental studies regarding the microwave heating on a helical configuration. The numerical simulations were performed using *COMSOL Multiphysics* and the results show that the helical configuration is a suitable way to increase the heating uniformity inside the tube due to the radial mixing. Gao et al. [12] studied the heating of a water film using microwaves in *COMSOL Multiphysics* and the authors report good agreement with experimental data, which further validates the electromagnetic and heat transfer interfaces available in this commercial software. D'Ambrosio et al. [13] study the design of overmoded resonant cavities, having the conversion efficiency from microwaves to thermal energy as the most important metric to optimize. The cavity spectrum (i.e. the dependency of the S_{11} parameter with frequency, which affects the power reflected in the sample and thus the heating efficiency) simulated in the commercial software is very similar to that obtained experimentally.

Microwave heating has emerged as a novel technology in other fields, such as pyrolysis of biomass [14,15], food drying [16] and water desalination [17]. Some of these studies focus on the numerical simulation of microwave heating through a coupled model [4,15,18]

Other works have dealt with the improvement of the heating efficiency and uniformity using non-conventional techniques: He et al. [19] used two rotary waveguides, studying the influence of the shape, position and material of the load; Zhu et al. [20] conducted a similar study, concluding that the COV decreases from 0.63 to 0.31 when a rotary radiation structure is used; Tang et al. [21] used frequency variation, which reveals to be an effective tool to improve the heating uniformity both in numerical simulations and experiments.

The International Energy Agency (IEA) predicts that the energy efficiency may be responsible for a reduction in the World energy consumption from 410 EJ in 2020 to 300 EJ in 2050 [22] (1 EJ = 10^{18} J). In this context, the application of optimization techniques to the microwave heating process has been applied to a wide variety of materials. Mechenova and Yakovlev [23] used a multivariable

optimization procedure to determine the set of design variables that guarantees the maximum efficiency. The results show that the method is highly efficient in the minimization of the reflection coefficient, requiring reasonable processing times and converging faster than the global optimization procedures (such as genetic algorithms). The same procedure is used by Moon and Yakovlev [24] to study the impact of the dielectric properties and dimensions of a dielectric insert in the heating uniformity in a microwave applicator. The procedure is successful in maximizing the heating uniformity as the relative standard deviation values associated to the combinations obtained by the procedure (about 20%) are much lower than the non-optimized points in the database (between 27% and 136%, 78% on average).

Mäkelä [25] presents a practical tutorial regarding the use of experimental design combined with response surface methodology (RSM). The model is also highly effective on predicting the response using values out of the original dataset, as long as those values are within the range used to build the model. On the other hand, Fan et al. [26] studied the optimization of the microwave induced carbonization of rapeseed shell, with bio-oil and bio-chart as the products. To enhance microwave heating, a susceptor (SiC) was used and the heat patterns as well as the product yield were optimized via RSM. The results indicate a good fit by the response surfaces to the experimental data.

In energy intensive industries, the most common microwave heating devices fall into two categories: conveyor belts and rotary kilns. Conveyor belts are commonly used in the food industry to heat food materials [27,28]. This technology is also frequently used in drying processes [28,29] and in the cement industry [30] to promote homogenization of the microwave energy inside the cavity.

Regarding the conventional heating in rotary kilns, these are used in the industry for a few decades [31,32], even in the pigment sector [33,34]. On the other hand, rotary kilns have been recently studied to attest their capabilities when combined with microwave heating as part of European Projects like DAPhNE [35] and the follow-up project DESTINY [36,37]. For example, Gonçalves et al. [38] numerically study the production of limestone through microwaves in a rotary kiln system. These systems are very popular due to their higher mixing capacity when compared to the conveyor belt system.

The production of pigments in a rotary kiln was addressed in Ramos et al. [39] for doped TiO_2, including chemical reactions and heat transfer. The proposed methodology outlined by Ramos et al. [39] contributes to the design of microwave heating devices. The calculation of both the electromagnetic and thermal efficiencies allows to understand where the major energy losses are occurring, simplifying the design of such reactors. The highest global efficiency was 54% for a mass flow rate of 2.26 kg/h in the three-dimensional case.

In this work, two different geometrical configurations are studied: the 2D configuration is virtually related with conveyor belt production line while the 3D geometry is directly related with the rotary kiln production. From the pigments with available dielectric properties [40], the Brown 24 pigment was chosen over other pigments due to its lower thermal conductivity and increasing loss tangent with temperature, which may pose problems during microwave heating, like thermal-runaways. As such, this material is a more challenging choice in the design and optimization of microwave cavities with numerical simulations, highlighting the benefits of the proposed optimization methodology.

The aim of this work is to optimize a microwave cavity that processes ceramic pigments and make the microwave technology more competitive. Moreover, this work aims at improving the heating of high loss tangent materials when chemical reactions occur at the same time. The ultimate objective is the decarbonization of energy intensive industries through the electrification of the heating source.

The novelty of this work consists at combining optimization techniques and automatic controllers with the numerical simulation of microwave processing at high temperatures, which is an unexplored issue in the Literature — as the majority of the works only cover microwave heating at low temperature and none of them includes ceramic pigments as the load. As far as the authors know, this is the first work addressing the modelling, simulation and optimization of high temperature continuous microwave reactors coupled with a MATLAB controller that guarantees maximum electromagnetic efficiency and total chemical conversion.

In Section 2, some theoretical insight regarding microwave heating is presented, namely the governing equations; in Section 3, the computational model is described, with an emphasis on the geometry and boundary conditions; in Section 4, the results are presented for the 2D and 3D geometries; and in Section 5, the main conclusions will be summarized.

2. Multi-physics model

In this section, the three physical interfaces (chemical, thermal and electromagnetic) will be briefly described, with an emphasis on the equations that are being solved for each interface.

2.1. Chemical model

Regarding the chemical species interface, the aim is to compute the local conversion degree (α). The conversion degree is a metric of how far the chemical reactions that conduct to the synthesis of the pigment are from the end (i.e. the total conversion state). The chemical model used in this work is the same used in the previous article of the authors [39]. As such, the details will be omitted for the sake of brevity.

As the chemical conversion of reactants into products is highly complex for the pigment studied, a global and simpler model assuming a one-step reaction mechanism was employed. The reaction mechanism adopted here is the JMAK model (also known as the Avrami equation) and the kinetic triplet used to compute the local source of the conversion degree was extracted from experimental data present in the Literature [39]. The model was also validated against that data and the numerical results were very similar to the experimental profiles [39].

The differential equation that describes the chemical species transport is given by Eq. (1) [41]. This equation assumes no diffusion and stationary regime ($\partial/\partial t = 0$, where t is the time [s]).

$$\rho(\mathbf{v}\cdot\nabla\alpha) = R = \rho\, k(T)\, f(\alpha) \tag{1}$$

where ρ represents the density [kg/m^3], $\mathbf{v}$ is the velocity vector [m/s], α is the conversion degree, R represents the source due to chemical reactions [kg/(m^3 s)], k indicates the reaction constant [s^{-1}], T represents the temperature [K] and $f(\alpha)$ is the kinetic model.

As it was mentioned before, the Avrami equation was used as the kinetic model, which is formally given by Eq. (2).

$$f(\alpha) = n(1-\alpha)[-ln(1-\alpha)]^{1-\frac{1}{n}} \tag{2}$$

where n represents the Avrami exponent.

The reaction constant is given by Eq. (3), which couples the reaction rate R to the local temperature T.

$$k(T) = k_0\, exp\left(-\frac{E_a}{RT}\right) \tag{3}$$

where k_0 represents the pre-exponential factor [s^{-1}], E_a indicates the activation energy [J/mol] and $R = 8.314$ J/(mol K) represents the universal gas constant.

2.2. Thermal model

Regarding the thermal model, the energy equation, given by Eq. (4), is solved to compute the temperature field within the domain [42].

$$\frac{\partial}{\partial t}(\rho C_p T) + \mathbf{v}\cdot\nabla(\rho C_p T) + \nabla\cdot(\dot{\mathbf{q}}'' + \mathbf{q}''_{rad}) = \dot{Q}'''_{chem} + \dot{Q}'''_{EM} \tag{4}$$

where C_p represents the specific heat at constant pressure [J/(kg K)], $\dot{\mathbf{q}}''$ represents the conduction heat flux [W/m^2], $\mathbf{q}''_{\mathbf{rad}}$ is the radiative heat

flux [W/m^2], $\dot{Q}'''_{chem}$ is the heat source due to chemical reactions [W/m^3] and $\dot{Q}'''_{EM}$ is the electromagnetic heat source [W/m^3]. The Fourier Law is used to compute the heat flux due to conduction: $\dot{\mathbf{q}}'' = -k\nabla T$, where k is the thermal conductivity [W/(m K)].

The Eq. (4) describes a differential (local) energy balance. On the left-hand side, this equation includes the transient term, the convective term and the conduction term, while on the right-hand side there is the net heat generation ($\dot{Q}$), that has contributions due to the chemical reactions and the electromagnetic heating.

Integrating Eq. (4), one obtains an integral (global) energy balance, which is given by the set of Eqs. (5).

$$B_0 + B_1 + B_{2a} + B_{2b} - B_3 - B_4 = 0 \tag{5a}$$

$$B_0 = \iiint_{CV} \frac{\partial}{\partial t}(\rho C_p T)\, dV \tag{5b}$$

$$B_1 = \iiint_{CV} \mathbf{v} \cdot \nabla(\rho C_p T)\, dV \tag{5c}$$

$$B_{2a} = \iint_{S_1} h(T - T_{ext})\, dA + \iint_{S_2} (-k\nabla T) \cdot \hat{\mathbf{n}}\, dA \tag{5d}$$

$$B_{2b} = -\iint_{S_3} \dot{q}''_{rad}\, dA \tag{5e}$$

$$B_3 = \dot{Q}_{EM} \tag{5f}$$

$$B_4 = \iiint_{CV} |\mathbf{v} \cdot \nabla\alpha|\,(-\Delta H)\,\rho\, dV \tag{5g}$$

where CV means 'control volume', h represents the convection coefficient [W/(m^{2}K)] on the boundaries where there is heat transfer by convection (i.e. boundaries denoted by S_1; the other boundaries are denoted by S_2), $T_{ext} = 293.15$ K is the ambient temperature, $\hat{\mathbf{n}}$ represents the exterior normal vector, q''_{rad} indicates the net radiative heat flux [W/m^2] in the exterior boundaries given by S_3, $\dot{Q}_{EM}$ represents the electromagnetic heat source [W] and ΔH indicates the enthalpy of reaction [J/kg]. The energy balance is formally given by Eq. (5a), where B_0 is the transient term [W], B_1 is the convective term [W], B_{2a} accounts for the thermal losses by convection [W], B_{2b} accounts for the thermal losses by radiation [W], B_3 quantifies the dissipated thermal energy from the electromagnetic interface [W] and B_4 is the term related to the power that is absorbed ($\Delta H > 0$) or released ($\Delta H < 0$) due to the chemical reactions [W].

Regarding the radiative heat transfer, the main equations will be presented as follows [42]. Considering an opaque surface at temperature T, the net radiative heat flux is given by the difference between the irradiation (the radiative flux that arrives to the surface, G) and the radiosity (the radiative heat flux that is going out of the surface, J):

$$\dot{q}''_{rad} = G - J \tag{6}$$

where $\dot{q}''_{rad}$ is the net radiative heat flux [W/m^2], G is the irradiation [W/m^2] and J is the radiosity [W/m^2].

The radiosity is given by the sum of the total emissive power of the surface and the portion of the irradiation that is reflected by the body:

$$J = \rho_s G + \epsilon_s e_b(T) \tag{7}$$

where ρ_s is the surface reflectivity (which is the portion of the irradiation that is being reflected by the surface), ϵ_s is the surface emissivity (defined as the ratio of the emissive power of the body at a given temperature T by the black body emissive power at the same temperature, given by $e_b(T)$ [W/m^2]).

Substituting Eq. (7) into Eq. (6), one obtains:

$$\dot{q}''_{rad} = G - J = (1 - \rho_s)G - \epsilon_s e_b(T) \tag{8}$$

If one assumes the body to be as an ideal grey body, then the absorptivity is equal to the emissivity ($\alpha_s = \epsilon_s$) [42]. As such, as the transmissivity is null, because the body is opaque, one obtains that $\alpha_s = 1 - \rho_s = \epsilon_s$. Consequently, the radiative heat flux becomes:

$$\dot{q}''_{rad} = \epsilon_s[G - e_b(T)] \tag{9a}$$

$$\dot{\mathbf{q}}''_{rad} = -\dot{q}''_{rad}\hat{\mathbf{n}} = -\epsilon_s[G - e_b(T)]\hat{\mathbf{n}} \tag{9b}$$

where $e_b(T) = n^2\sigma T^4$, which is the Stefan–Boltzmann law, being n the refractive index of the medium ($n = 1$ was used for air) and $\sigma = 5.67 \times 10^{-8}$ W/(m^2 K^4) is the Stefan–Boltzmann constant.

Eq. (8) is used as a radiative boundary condition for the boundaries that are in the interface between an opaque body and a transparent medium (such as the air). The heat flux $\dot{q}_{rad}$ is used as a source term in the energy equation so that the radiation heat transfer is being accounted for.

The irradiation (G) is the sum of the ambient irradiation (G_{amb}, from the surroundings) and the mutual irradiation (G_m, from the other surfaces). For a given element i, the mutual irradiation will have contributions from all the other elements j, depending on the corresponding view factor between each pair of surfaces:

$$G_{m,i} = \sum_{j=1}^{N} F_{ij} J_j \tag{10}$$

where F_{ij} is the view factor between the surfaces that contain the elements i and j.

The radiosities can finally be determined by substituting Eq. (10) into Eq. (7):

$$J_i = (1 - \epsilon_{s,i})\left(\sum_{j=1}^{N} F_{ij} J_j + G_{amb}\right) + \epsilon_{s,i} n^2 \sigma T_i^4 \tag{11}$$

where $G_{amb} = F_{amb} n^2 \sigma T_{amb}^4$ is a known quantity once the view factor for the surroundings (F_{amb}) is determined and $T_{amb} = 293.15$ K is the surroundings temperature.

Eq. (11) is an implicit relation between the radiosity on a given element i and the radiosities on the other elements j. This equation, applied to all the elements that have non-zero mutual radiation, allows to relate the radiosities.

Note that the temperature appears in the independent term of Eq. (11) and the radiosities also appear in the energy equation (because q''_{rad} in Eq. (9a) is used as a source in the energy equation). Hence, Eq. (11) needs to be solved simultaneously with the energy equation to determine the temperature and the radiosities in each element (i.e. the radiative heat flux associated to each element).

2.3. Electromagnetic model

The electromagnetic interface comprises the determination of the electric and magnetic field by solving the Maxwell's equations, given by the set of Eqs. (12) [43].

$$\nabla \times \mathbf{E} = -\frac{\partial \mathbf{B}}{\partial t} \tag{12a}$$

$$\nabla \times \mathbf{H} = \frac{\partial \mathbf{D}}{\partial t} + \mathbf{J} \tag{12b}$$

$$\nabla \cdot \mathbf{D} = \rho_c \tag{12c}$$

$$\nabla \cdot \mathbf{B} = 0 \tag{12d}$$

where $\mathbf{E}$ represents the electric field [V/m], $\mathbf{B}$ indicates the magnetic flux density [Wb/m^2], $\mathbf{H}$ represents the magnetic field [A/m], $\mathbf{D}$ indicates the electric flux density [C/m^2], $\mathbf{J}$ represents the electric current density [A/m^2] and ρ_c represents the electric charge density [C/m^3].

The electric flux density $\mathbf{D}$, the magnetic flux density $\mathbf{B}$ and the electric current density $\mathbf{J}$ can be related to the computational variables

(the electric and magnetic fields, **E** and **H**, respectively) through the constitutive relations, given by Eqs. (13).

$$\mathbf{D} = \epsilon\mathbf{E} \tag{13a}$$

$$\mathbf{B} = \mu\mathbf{H} \tag{13b}$$

$$\mathbf{J} = \sigma\mathbf{E} \tag{13c}$$

where the electric permittivity is given by $\epsilon = \epsilon' - j\epsilon''$ [F/m], the magnetic permeability is given by $\mu = \mu' - j\mu''$ [H/m] and σ represents the electric conductivity [S/m] of the material.

The Maxwell's equations may be combined with the constitutive relations to relate all the variables with the electric field **E**, obtaining the Helmholtz equation — given by Eq. (14).

$$\nabla \times \frac{1}{\mu_r}(\nabla \times \mathbf{E}) - k_0^2\left(\epsilon_r - \frac{j\sigma}{\omega\epsilon_0}\right)\mathbf{E} = \mathbf{0} \tag{14}$$

where $\epsilon_r = \epsilon/\epsilon_0$ represents the relative dielectric permittivity, $\mu_r = \mu/\mu_0$ indicates the relative magnetic permeability, $k_0 = \omega\sqrt{\mu_0\epsilon_0}$ represents the vacuum wave number $[m^{-1}]$, $\epsilon_0 = 8.854 \times 10^{-12}$ F/m indicates the dielectric permittivity in vacuum, $\mu_0 = 4\pi\times10^{-7}$ H/m represents the magnetic permeability in vacuum, ω indicates the angular frequency [rad/s] and $j = \sqrt{-1}$ is the imaginary unit.

The electric permittivity (ϵ) and the magnetic permeability (μ) may be complex numbers: the real part of these quantities refers to the ability of the material to store electric or magnetic energy, respectively; on the other hand, the imaginary part accounts for the losses due to damping of the electric or magnetic dipole moments [44] within the medium, respectively. In the present case, the magnetic dissipation was not considered ($\mu'' = 0$) and the Joule effect due to conduction was included in the complex permittivity. As such, the total heat generation is given by Eq. (15).

$$\dot{Q}_{EM} = \iiint_{CV} \frac{\omega\epsilon''}{2}|\mathbf{E}|^2\, dV \tag{15}$$

where the electric field norm is given by $|\mathbf{E}|$ [V/m].

The penetration depth (δ) is defined by the distance from the surface of the medium at which the electric field norm drops to $1/e$ (approximately 37%) of its value at the surface. This variable is a measure of the attenuation of the electric field in the medium and is given by Eq. (16).

$$\delta = \frac{c_0}{2\pi f\sqrt{2\epsilon_r'}}\left\{\left[1 + \left(\frac{\epsilon_r''}{\epsilon_r'}\right)^2\right]^{0.5} - 1\right\}^{-0.5} \tag{16}$$

where $c_0 = 1/\sqrt{\mu_0\epsilon_0}$ represents the speed of light in vacuum [m/s] and f indicates the frequency $[s^{-1}]$.

2.4. Coupling

The three physical interfaces earlier introduced interact with each other, making the model highly coupled and non-linear. The dissipated heat is obtained from the electromagnetic interface (Eq. (15)) and affects the energy equation. Moreover, the dielectric permittivity is highly dependent on temperature.

On the other hand, the reaction constant k also depends on temperature (Eq. (3)) and the chemical reactions may produce/release heat that has to be accounted for in the energy equation (via Eq. (5g)). The major dependencies between the three physical interfaces are summarized in Fig. 1.

3. Computational domain

In this section, the main features of the model will be presented, with an emphasis on the description of the geometry and the boundary conditions.

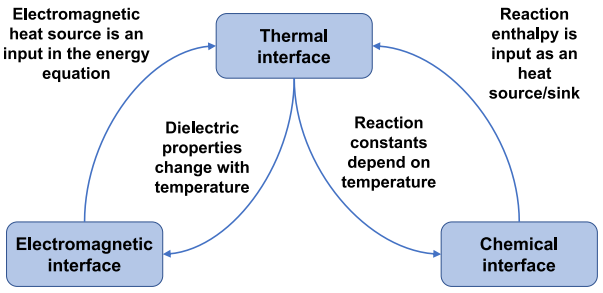

Fig. 1. Dependencies between physical interfaces.

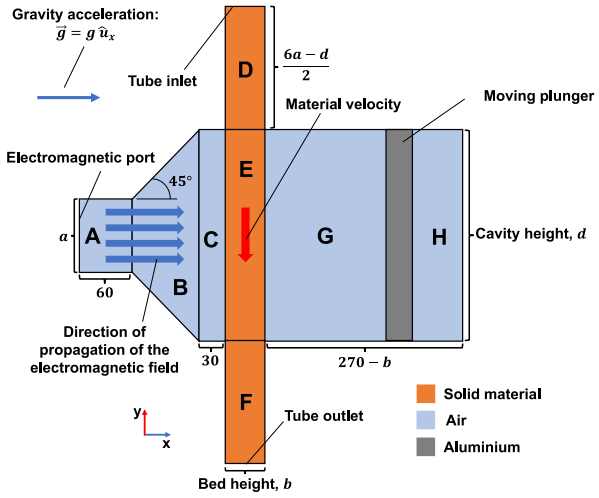

Fig. 2. Conveyor belt: schematic representation of the 2D cavity used in the model. In the present model, $a = 86.36$ mm and all the dimensions are in mm. The parameters b and d will be part of the parametric study carried out in Section 4.

3.1. Model geometry

Concerning the bidimensional case, the geometry is represented in Fig. 2, where it is possible to see the relative position between the electromagnetic port and the load as well as the different materials that were used in the model. The material enters at the inlet, in sub-domain D, and exits at the outlet, in sub-domain F. The material flows vertically in the figure and the electromagnetic field propagates in the normal direction to the flow. Note that the figure is rotated and the gravitational acceleration is horizontal in this representation. Some dimensions are presented (in mm) and the parameters b (bed height) and d (cavity height) will be defined latter as they will be changed during the parametric study.

The 2D geometry intends to simulate the production of the pigment in a conveyor belt, where the material velocity has only an axial component. The geometry shows the medium plane of the cavity, which is crossed by a conveyor belt, where the bed material is being processed. It was assumed no variation of the computational variables in the z-direction ($\partial/\partial z = 0$). Since the waveguide is operating in the TE_{10} mode, we have that $E_x = E_y = 0$ and $\partial E_z/\partial z = 0$; for the magnetic field, $H_z = 0$ and $\partial H_x/\partial z = \partial H_y/\partial z = 0$. As such, there is no variation of the electromagnetic field in z-direction, which justifies the 2D assumption. Concerning the thermal and chemical interfaces, the local variations are also zero in the z-direction since the plane shown in Fig. 2 is a symmetry plane, again justifying the 2D approach.

Concerning the 3D case, the geometry is presented in Figs. 3a and 3b, showing the rectangular cavity being crossed by a circular tube. The tube is partially filled with the material with a filling angle Γ (see Fig. 3b). The main geometrical parameters are summarized in Table 2.

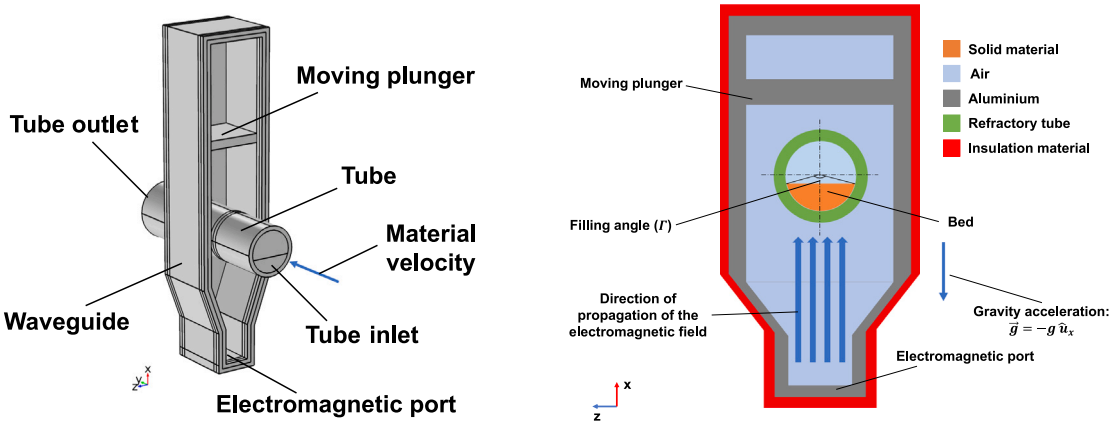

(a) $3D$ geometry with some waveguide walls hidden. The geometrical parameters are summarized in table 2.

(b) $2D$ cut representation inside the waveguide – Oxz plane in figure b).

Fig. 3. Rotary kiln: schematic representation of the 3D cavity used in the model.

Table 2
Geometrical parameters of the 3D geometry.

Parameter	Value
Tube internal diameter – D_i [mm]	20–35
Tube thickness [mm]	7
Tube length – L [mm]	300
Filling angle – Γ [°]	150
Cavity length [mm]	566
Cavity thickness [mm]	7
Plunger thickness [mm]	15

The tube is rotating and the material flows from the inlet to the outlet. The cavity and the tube outlet are insulated with an insulation material, shown in red in Fig. 3b.

The choice of these two geometries is understandable as these configurations are the most common in industrial microwave heating devices: the conveyor belt configuration is more common in the food industry and in drying processes and the rotary kiln is preferred in the steel and cement sectors. As the high temperature microwave processing of pigments is still an evolving field, it is beneficial to keep the design of these devices as comprehensive as possible. For this reason, both configurations were studied and compared.

In both the 2D and the 3D case, the cavity is filled with static air at the atmospheric pressure. The rectangular waveguide WR-340 (with a cross section $a \times b = 86.36 \times 43.18$ [mm^2]) is used, operating at $f = 2.45$ GHz. A moving plunger is also used to change the cavity length to put the electromagnetic field peak on top of the material in the reaction zone (which is defined as the portion of the tube that is inside the waveguide). Hence, the plunger allows to automatically tune the impedance of the cavity, maintaining the heating efficiency at its maximum. The position of the plunger is chosen by a controller developed in *MATLAB*, which will be addressed latter in this article.

It is worthwhile mentioning that the plunger is assumed to be perfect, which means that the magnetic flux across it is null (no magnetic leakage through the plunger). This is a common practice in the Literature [45]. This approach is considered realistic since the gap between the plunger and the waveguide walls is much smaller than the cut-off distance (which is half of the wavelength inside the waveguide). This means that the cut-off phenomenon will strongly attenuate the field in the area between the plunger and the waveguide. Moreover, filters may also be used to effectively eliminate the leakage in a microwave device [46].

3.2. Domains and boundary conditions

The equations solved for each interface were already presented in Section 2: Eq. (1) is solved in the chemical interface; Eq. (4) – the energy equation – for the thermal one; and Eq. (14) – the Helmholtz equation – for the electromagnetic interface.

The chemical interface is only solved in the bed material as this is the only sub-domain where chemical reactions are being considered. The electromagnetic interface is solved for every point in the area between the electromagnetic port and the moving plunger. Finally, the thermal interface is solved all over the domain. As an example, in the 2D case, the chemical interface is solved for sub-domains D, E and F; and the Helmholtz equation is solved for domains A, B, C, D, E, F and G (see Fig. 2).

The boundary conditions, for the chemical interface, are:

1. **Prescribed conversion degree**: $\alpha = 0.001$ at the inlet, meaning the absence of products and the existence of reactants;
2. **Outflow**: $\mathbf{n} \cdot \nabla\alpha = 0$ at the outlet, meaning that the chemical transport occurs only via convection;
3. **No flux**: $-\mathbf{n} \cdot \nabla(\rho \mathbf{v} \alpha) = 0$ at the remaining boundaries, meaning that there is no transport across those boundaries.

For the thermal interface, the boundary conditions are:

1. **Prescribed temperature**: $T = 300$ K at the inlet, meaning that the reactants enter at ambient temperature;
2. **Adiabatic boundary**: $-\mathbf{n} \cdot \dot{\mathbf{q}}'' = 0$ at the outlet, assuming that the temperature field would not change after exiting the tube;
3. **Convective boundary**: $-\mathbf{n} \cdot \dot{\mathbf{q}}'' = \dot{q}''_{conv} = h(T_{ext} - T)$ at the remaining boundaries, meaning that there is heat transfer through convection in those boundaries. $T_{ext} = 293.15$ K is the exterior temperature; in the 3D case, the convection coefficient h was computed assuming free convection [39], while in the 2D case the average value $h = 2.5$ W/(m^2 K) was used;
4. **Diffuse surface**: $-\mathbf{n} \cdot \dot{\mathbf{q}}'' = \dot{q}''_{rad} = \epsilon_s[G_m + F_{amb} n^2 \sigma T_{amb}^4 - e_b(T)]$ at the boundaries that are in the interface between an opaque body and a transparent medium (i.e., the air). This boundary condition accounts for radiative heat transfer on those boundaries.

Note that the boundary conditions 3 and 4 for the thermal interface represent the energy balance applied to a surface where pure convective or pure radiative heat transfer is occurring, respectively.

For the electromagnetic interface, the following boundary conditions were used:

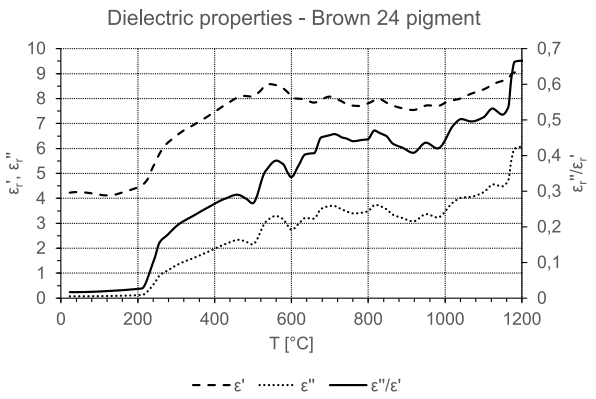

Fig. 4. Temperature dependence of the pigment dielectric properties [40].

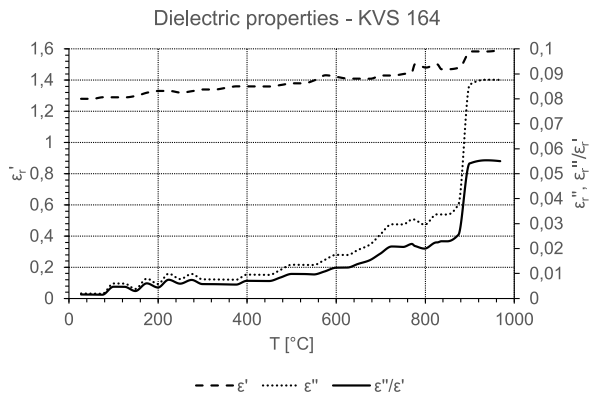

Fig. 5. Temperature dependence of the tube dielectric properties [47].

1. **Port**: this condition was applied to the electromagnetic port (see Figs. 2 and 3) and assumes that there is wave excitation;
2. **Perfect electric conductor**: $\mathbf{E} \times \mathbf{n} = \mathbf{0}$ at the remaining boundaries. This condition assumes the waveguide walls reflect all the incident wave, without absorbing or transmitting any electromagnetic radiation.

Finally, the initial conditions prescribed are:

1. $\alpha = 0.001$ for the chemical interface, meaning the presence of reactants and the absence of products;
2. $\mathbf{E} = \mathbf{0}$ for the electromagnetic interface;
3. a linear temperature profile between the inlet of the tube (at $T = 300$ K) and the outlet of the reaction zone (at $T = 1100$ K in the 2D case and $T = 1800$ K in the 3D case).

3.3. Physical properties

For the sake of conciseness, the physical properties of the pigment and the chemical model used to predict the conversion degree are summarized in the previous work published by the authors [39]. The dielectric properties are represented in Fig. 4, which shows the temperature dependence of both the real and imaginary parts of the dielectric permittivity [40]. The loss tangent, given by the ratio of the real part to the imaginary part ($tan(\delta) = \epsilon_r''/\epsilon_r'$), is also presented. The electric conductivity was set to zero ($\sigma = 0$ S/m) as the losses associated to the Joule effect were taken into account in the imaginary part of the permittivity.

The tube was considered to be made from KVS-164, a low loss refractory material made of 65% alumina (Al_2O_3) and 34% silica (SiO_2). This material exhibits low absorption of microwave energy at high temperatures and is highly recommended for microwave applications [47]. The dielectric properties are presented in Fig. 5, which clearly shows that the material is practically transparent to the electromagnetic field, as the loss factor is very close to zero.

Regarding the thermal properties, the specific heat was computed based on the composition, according to Eq. (17):

$$C_{p,tube} = 0.65\, C_{p,Al_2O_3} + 0.34\, C_{p,SiO_2} \tag{17}$$

The specific heats of alumina and silica were computed based on Eq. (18) [48]:

$$C_p = 4.1868\,(a + 10^{-3}\, b\, T + 10^{5}\, c\, T^{-2}) \tag{18}$$

where a, b and c are constants that can be found in Table 3 for the chemical species involved [48].

The thermal conductivity of the tube is shown in Fig. 6 and its density was set to $\rho_{tube} = 300$ kg/m^3 [49].

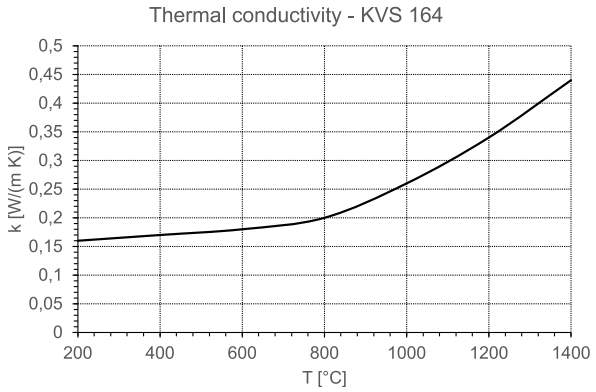

Fig. 6. Temperature dependence of the tube thermal conductivity [49].

Table 3
Input parameters used to compute the specific heats of both alumina and silica, according to Eq. (18) [48].

Species	a	b	c	Range [K]
$SiO_2 - \alpha$	10.49	0.24	−1.44	298–84
$SiO_2 - \beta$	14.08	2.40	0.00	848–2000
Al_2O_3	25.48	4.25	−6.82	298–2072

Finally, the *MATLAB* controller used in this work is the same used in previous works of the authors [39], where the reader may find all the details. The controller was adapted from the works published in [50,51]. The input power is computed using Eq. (19), which imposes stationary regime ($\partial/\partial t = 0$) and total chemical conversion.

$$P_{port} = \frac{B_1 + B_{2a} + B_{2b} - 0.999\,\dot{m}\,(-\Delta H)}{\eta_{EM}} \tag{19}$$

where P_{port} is the input power [W], the convective term B_1 is calculated with Eq. (5c), the thermal losses terms B_{2a} and B_{2b} are determined using Eqs. (5d) and (5e), respectively, $\dot{m}$ is the mass flow rate [kg/s] and η_{EM} is the electromagnetic efficiency.

3.4. Key performance indicators (KPI)

The key performance indicators (KPI) used in this work will be briefly introduced in this sub-section. The electromagnetic efficiency, given by Eq. (20), comes from the electromagnetic energy balance and reflects the ability of the load to absorb electromagnetic energy and dissipate it into heat. Thus, the electromagnetic efficiency increases as the reflected power decreases.

$$\eta_{EM} = 1 - |S_{11}|^2 = \frac{\dot{Q}_{EM}}{P_{port}} \tag{20}$$

where η_{EM} is the electromagnetic efficiency and S_{11} is the fraction of the input power that is reflected from the load. For a single port device, this parameter is measured through the portion of the electromagnetic field that returns to the port after the interaction with the load.

The thermal efficiency is a metric of how efficient is the absorbed power used to increase the temperature of the system. This KPI is defined in Eq. (21), as the ratio of the convective term (interpreted here as the useful component of the absorbed power) by the total heat generation (including the heat released during the chemical reactions).

$$\eta_T = \frac{B_1}{\dot{Q}_{EM} + B_4} \tag{21}$$

where η_T is the thermal efficiency, B_1 is the convective term [W] defined in Eq. (5c), $\dot{Q}_{EM}$ is the absorbed power [W] defined in Eq. (15) and B_4 is the heat released [W] during the chemical reactions, defined by Eq. (5g).

The global efficiency, given in Eq. (22) by the product of the electromagnetic and the thermal efficiencies, is a metric of the overall performance of the microwave reactor, including both the electromagnetic and thermal phenomena.

$$\eta_G = \eta_{EM}\,\eta_T \tag{22}$$

where η_G is the global efficiency.

The specific energy consumption, introduced in Eq. (23), gives the amount of energy necessary to produce 1 kg of pigment and is thus a useful metric to compare the pigment production under different conditions.

$$C_e = \frac{P_{port}}{\eta_M\,\dot{m}} \tag{23}$$

where C_e is the specific energy consumption [J/kg] and $\eta_M = 0.85$ [44] is the magnetron efficiency, which quantifies the efficiency conversion from electricity to microwaves. $\dot{m} = \rho\,A\,v$ is the yield (i.e., the mass flow rate) [kg/s], where $\rho = 3931.1$ kg/m^3 is the pigment density, A is the cross section area [m^2] and v is the axial solids velocity [m/s].

The average heat source is given by Eq. (24a) and the heat source standard deviation is defined in Eq. (24b). The standard deviation is a metric of how the heat source deviates from the mean value and quantifies the heating uniformity inside the reactor.

$$\overline{\dot{Q}'''}_{EM} = \frac{1}{V}\iiint_{CV} \dot{Q}'''_{EM}\,dV \tag{24a}$$

$$\sigma(\dot{Q}'''_{EM}) = \sqrt{\frac{1}{V}\iiint_{CV} (\dot{Q}'''_{EM} - \overline{\dot{Q}'''}_{EM})^2\,dV} \tag{24b}$$

$$\dot{Q}'''_{EM} = \frac{\omega\,\epsilon''}{2}|\mathbf{E}|^2 \tag{24c}$$

where $\overline{\dot{Q}'''}_{EM}$ is the average heat source [W/m^3], V is the volume in the reaction zone [m^3], $\dot{Q}'''_{EM}$ is the local heat source [W/m^3] and $\sigma(\dot{Q}'''_{EM})$ is the heat source standard deviation [W/m^3].

3.5. Solution procedure

The present results were obtained by solving the mathematical model described in Section 3 together with the boundary conditions and material properties depicted in Section 2. Whether for the 2D or 3D case, the procedure is the same: the electromagnetic, temperature and conversion degree fields are initialized according to the initial conditions showed in Section 2 and a transient computation is done until steady state conditions are obtained, following the pseudo-transient method. While marching in time, the plunger position is chosen at pre-defined time instants, depending on the temperature field at that instant. The solution is then assumed to be converged when the conversion degree is close to unit at the exit of the tube (in this case $\alpha > 0.999$ was considered, to account for a tolerance) and when the term B_0 from the energy balance equation (see Eq. (5b)) is less than a predetermined fraction of the electromagnetic heat source ($B_0/\dot{Q}_{EM} < 5\%$ was considered).

Regarding the plunger adjustment, the main idea is to restrict the length of the cavity in such a way that the electromagnetic field peak remains on top of the load (i.e., the pigment). At the beginning of the simulation, all plunger positions are tested and the one that gives the highest efficiency is chosen. Since the dielectric properties vary significantly with temperature, then the impedance of the cavity will also vary with time. This means that the position of the plunger that guarantees the maximum efficiency may vary with time. As a consequence, periodic checks are done by the controller to test if the current position is still the one that maximizes the heating efficiency. If this is not the case, the MATLAB controller performs additional electromagnetic simulations with constant temperature to check the plunger position that yields the maximum efficiency for the current temperature field.

An example of how the electromagnetic efficiency changes with the plunger position is given in Appendix, Fig. 20a. Moreover, a flowchart of the controller algorithm is also shown in the same appendix, see Fig. 20b.

4. Results and discussion

4.1. 2D results — conveyor belt

The results of this section are obtained for the bidimensional case of Fig. 2, for the conveyor belt configuration. The set of Figs. 7a-f presents the results obtained for the global, electromagnetic and thermal efficiencies, as well as the input power, the maximum temperature and the heat source standard deviation, respectively.

4.1.1. Influence of the cavity height, d

Fig. 7a shows one of the main advantages of having an opening of the cavity in the direction perpendicular to the direction of propagation of the electromagnetic field: the global efficiency increases significantly with d, specially for the higher bed heights, for which the increase may reach 15%.

One of the consequences of increasing the global efficiency for higher cavity heights is the reduction of the input power, as can be seen in Fig. 7d. Note that the mass flow rate is independent of the cavity height, which means that the same amount of material is being processed using lower amounts of energy per unit time, contributing to a higher global efficiency.

The increase in the global efficiency is clearly due to a higher electromagnetic efficiency, as can be seen in Fig. 7b. As such, increasing the value of d has a much more significant effect on the electromagnetic interface than on the thermal one, as the thermal efficiency remains practically constant for all values of d — see Fig. 7c.

The reasons that contribute to an increase of the electromagnetic efficiency with d can be found by inspecting the distribution of the absorbed power (Figs. 8a and 9a). In this figures, one may conclude that the absorbed power assumes a more volumetric distribution for the higher value of d, leading to higher electromagnetic efficiencies.

These results are consistent with the heat source standard deviation ($\sigma(\dot{Q}'''_{EM})$), which is a measure of the heating uniformity and is presented in Fig. 7f. This figure shows that the heat source assumes a less dispersive behaviour for higher cavity heights, which thus exhibit higher heating uniformity.

The volumetric heating is promoted by a low temperature region in the entry of the reaction zone, which is much wider for the higher values of d (as can be seen in Figs. 8b and 9b, which shows the temperature field obtained for both geometries). This low temperature region is associated to lower loss tangent values, making the thermal load more permeable to the electromagnetic field in that region — see Figs. 8c and 9c, which show the electric field distribution for the lowest

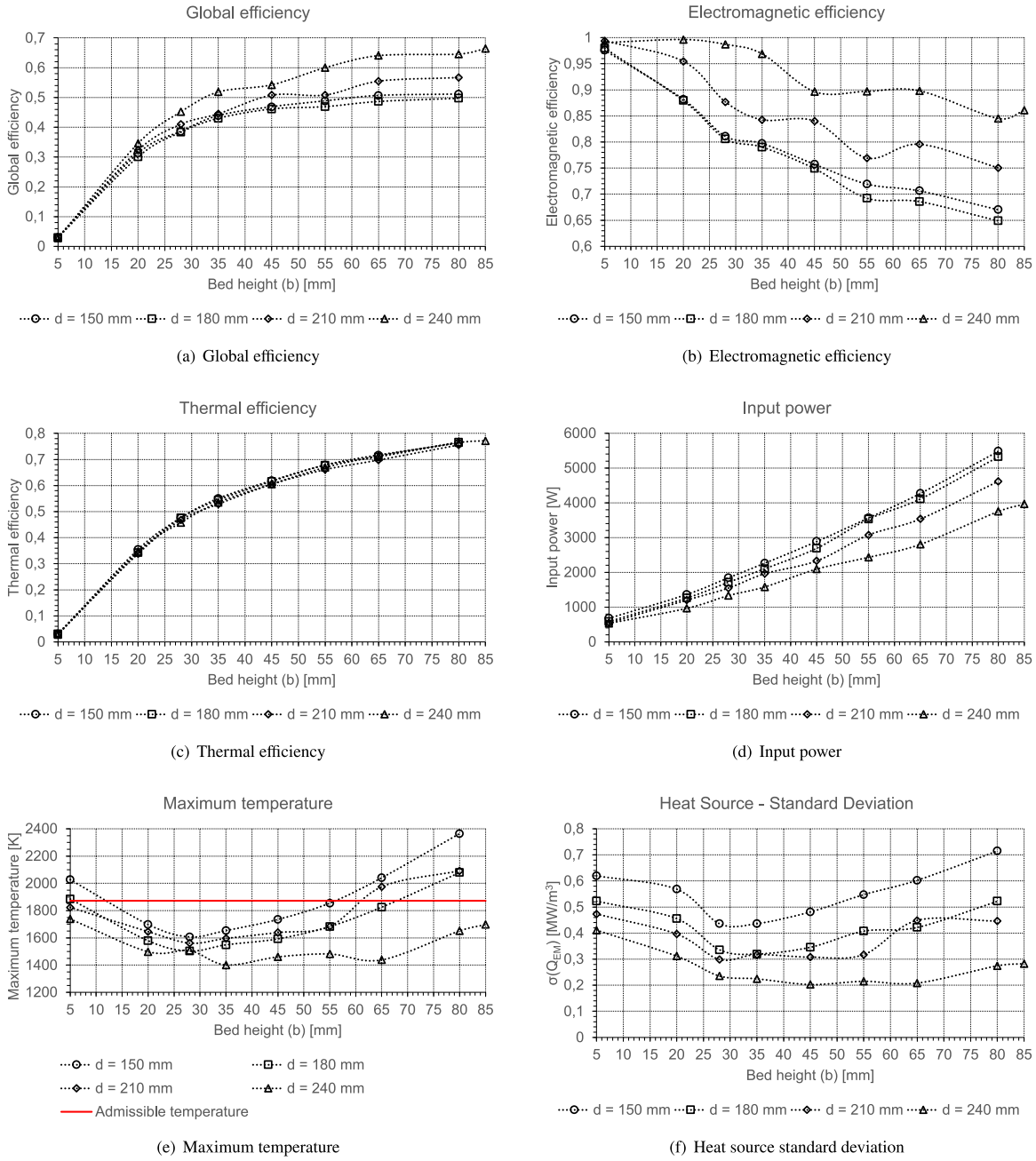

(a) Global efficiency

(b) Electromagnetic efficiency

(c) Thermal efficiency

(d) Input power

(e) Maximum temperature

(f) Heat source standard deviation

Fig. 7. Results obtained for the bidimensional case, namely the dependence of several variables on the cavity height (d) and the bed height (b).

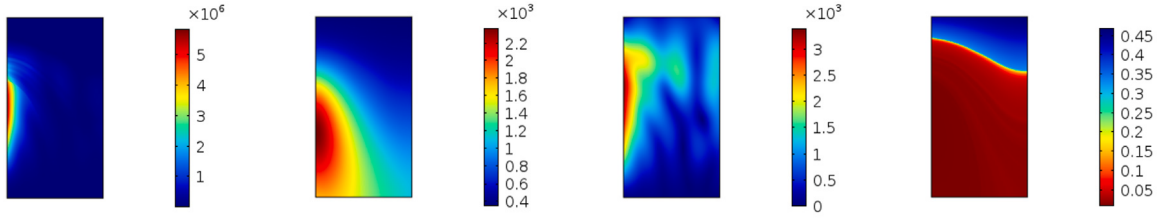

(a) Heat source

(b) Temperature

(c) Electric field norm

(d) Penetration depth

Fig. 8. Representation of several properties for $d = 150$ mm ($b = 80$ mm). Only region E is shown here (see Fig. 2).

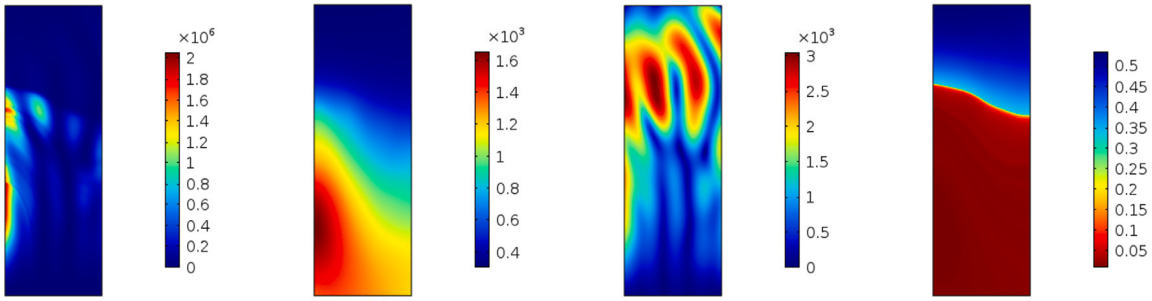

(a) Heat source (b) Temperature (c) Electric field norm (d) Penetration depth

Fig. 9. Representation of several properties for $d = 240$ mm ($b = 80$ mm). Only region E is shown here (see Fig. 2).

and highest cavity heights. Consequently, for higher cavity heights, the electromagnetic field penetrates deeper in the bed and attacks it by two fronts, contributing to a more volumetric heating.

This feature can be further corroborated by inspecting the penetration depth distribution over the reaction zone, which is shown in Figs. 8d and 9d. In this figures, it is quite clear that the low temperature region, where the loss tangent is smaller, is associated to high penetration depths, which causes the electric field to penetrate deeper in the bed. For the highest cavity height, the region where the penetration depth is higher becomes wider, making the heating more volumetric and increasing the electromagnetic efficiency. By comparing Figs. 9c and 9d, it is possible to note that the region where the electric field norm is higher is the same region where the penetration depth is increased, due to the lower local attenuation of the field.

The electromagnetic heating of high loss tangent materials poses a serious problem because of the superficial heating caused by the attenuation of the electric field in the load [39]. This problem is aggravated when the loss tangent increases with temperature as a thermal runaway may occur more frequently. Moreover, when a specified value of temperature is to be attained in all regions of the bed, the superficial heating may lead to higher maximum temperatures, because the difference between the maximum and the average temperatures increases with the heating heterogeneity [39]. This is the case when chemical reactions are being considered, as the local temperature must reach the reaction temperature so that the chemical reactions occur completely. Having this into account, the electromagnetic heating of high loss tangent materials that undergo chemical reactions is usually associated with very high temperatures, which may jeopardize the product quality or even damage the apparatus.

Fig. 7e shows another advantage of increasing the cavity height, which is the reduction of the maximum temperature of the bed. As such, besides the increase in the global efficiency of the process and the load heating uniformity, increasing the cavity height contributes to a better product and to a lower risk of melting the reactants that are used to produce the pigment, which is a common problem in microwave heating.

4.1.2. *Influence of the bed height, b*

Regarding the influence of the bed height (b), the first conclusion that is possible to achieve is the significant increase of the global efficiency with b, as shown in Fig. 7a. Although the electromagnetic efficiency decreases with b (Fig. 7b), the thermal efficiency increases very significantly with increasing b (Fig. 7c) and dominates the overall behaviour of the global efficiency.

The dependence of the thermal efficiency on the bed height is explained through the balance between the heat generation inside the domain and the heat dissipation through the boundaries. Considering a bidimensional case, the heat generation is a surface phenomenon, being proportional to the surface area of the domain; on the other hand, the dissipation of heat on the boundaries is proportional to the total length of the boundaries (i.e. the perimeter).

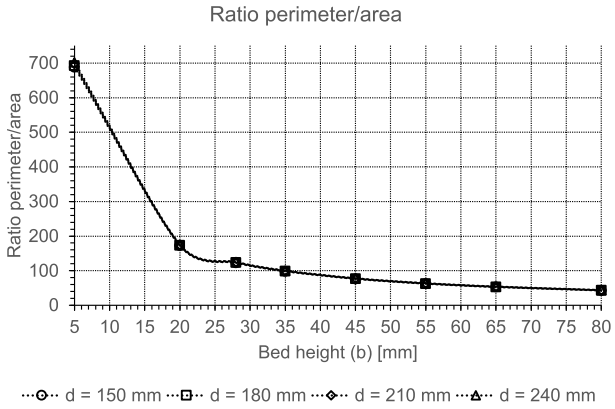

Fig. 10. Dependence of the ratio perimeter/area on the cavity height (d) and the bed height (b).

Fig. 10 shows the ratio perimeter/area for the cases presented so far. This figure allows to conclude that the geometries for which the ratio perimeter/area is higher exhibit lower thermal efficiencies. This is the case for the lower bed heights, for which the heat generation is practically equal to the thermal losses, leading to an inefficient use of the absorbed energy. As the bed height increases, the surface area also increases and the heat generation becomes more dominant when compared to the heat dissipation on the boundaries. Consequently, for the higher values of b, the ratio perimeter/area decreases and the thermal efficiency increases significantly.

Note that the perimeter/area ratio only depends on the bed height (b), being practically independent of the cavity height (d). This behaviour is also observed for the thermal efficiency (Fig. 7c), which further reinforces the importance of the perimeter/area ratio on the thermal analysis of the system.

Regarding the electromagnetic efficiency, it is possible to observe its reduction with b in Fig. 7b. The reduction of the electromagnetic efficiency for higher bed heights is justified by the attenuation phenomenon that occurs in a dissipative load. When the electromagnetic field propagates in a material having a non-zero loss tangent, some of the electromagnetic energy is converted into heat and the electric field norm decreases in the direction of propagation. The penetration depth (δ), introduced before and given by Eq. (16), is one of the metrics used to quantify the attenuation of the field.

Fig. 11 shows the evolution of the ratio δ_{min}/b with the cavity height (d) and the bed height (b). In this figure, δ_{min} is the minimum penetration depth observed in the reaction zone of the bed.

It is possible to conclude that this ratio decreases significantly for higher values of b, being around 0.1 for $b = 80$ mm. This means that the field is propagating inside a medium where the characteristic length in the direction of propagation (b) is one order of magnitude higher than

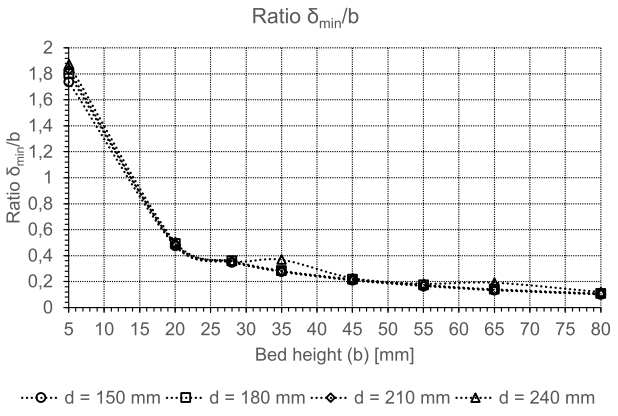

Fig. 11. Dependence of the ratio δ_{min}/b on the cavity height (d) and the bed height (b). δ_{min} is the minimum penetration depth observed in the reaction zone of the bed.

the minimum penetration depth observed in the load, which leads to a very strong attenuation of the field. Consequently, there is a wider region where the electric field norm is very low, as the electric field drops to about 37% only in the first 8 mm of propagation (according to the definition of penetration depth introduced before).

For lower values of b, the dimensions of the load are of the same order of magnitude of the minimum penetration depth, which makes the electric field norm to decrease less in the direction of propagation. As such, the heat dissipation occurs through all the regions of the bed, reducing the superficial effects of the microwave heating and increasing the electromagnetic efficiency.

Fig. 7e shows that the maximum temperature increases for both the lowest and the highest bed heights. Regarding the lower values of b, the temperature increases significantly because the bed is too thin, making the volumetric heat source very high and leading to very high maximum temperatures.

For the higher values of b, the reason is related to the total conversion condition together with the superficial heating that occurs for these geometries. When the heating becomes more superficial, the temperature field gets more heterogeneous. As the controller imposes total conversion for all geometries, the maximum temperature will increase for the higher values of b to increase the local temperature in the regions of the bed more distant to the electromagnetic port. In those regions, the temperature is the lowest but has to be higher than the reaction temperature, to ensure that the total conversion requisite is fulfilled. As such, the temperature in the regions closer to the electromagnetic port will arise drastically, which justifies the maximum temperatures obtained for higher bed heights. The low thermal conductivity of the pigment ($k = 0.5$ W/(m K)) contributes to a higher difference between the average and the maximum temperature, aggravating the increase of the latter to ensure the total conversion.

4.1.3. Constrained optimization

The profiles presented in Fig. 7e may be used in a constrained optimization problem to choose the best configuration from the ones presented in the graph. From this graph, it is possible to see that the maximum temperature values obtained are within the range 1400–2400 K. In order to avoid the melting of the product and damage the apparatus, it is recommended that the maximum temperature should be less than an admissible temperature, which is chosen according to the refractory used in the experimental apparatus. For KVS-164, the refractory material considered in this study, the maximum service temperature is about 1873 K. This value was chosen as the admissible temperature and is marked with red in Fig. 7e.

For each cavity height (d), the value of b that leads to the highest global efficiency while respecting the criterion $T < T_{adm} = 1873$ K must be chosen. The optimization problem is then formally defined by the set of Eqs. (25).

Table 4
Results obtained for the constrained optimization problem. b_{opt} is the bed height, from the ones studied in this work, that is a solution of the optimization problem defined by Eq. (25).

d [mm]	b_{opt} [mm]	η_G [%]
150	55	48.8
180	65	48.7
210	55	50.8
240	**85**	**66.4**

$$\begin{aligned} &\text{maximize } \eta_G \\ &\text{subject to} \\ T_{max,i} < T_{adm} = 1873 \text{ [K]} \\ \alpha_s > 0.999 \\ 5 \le b \le 85 \text{ [mm]} \\ 150 \le d \le 240 \text{ [mm]} \end{aligned} \tag{25}$$

where $T_{max,i}$ is the maximum temperature, $T_{adm} = 1873$ K is the maximum admissible temperature and α_s is the conversion degree at the outlet.

Note that the global efficiency increases monotonically with the bed height b, which means that the highest global efficiency will be associated to the highest value of b. This characteristic of the problem is specially useful since it avoids a compromise between mass flow rate and global efficiency — the highest mass flow rate and the highest global efficiency are obtained for the same geometry.

Table 4 presents the results obtained for the constrained optimization problem described by the set of Eqs. (25). In this table, b_{opt} is the bed height, from the ones studied in this work, that is a solution of the optimization problem defined by Eq. (25).

The results show that for the lower cavity heights d, the temperature condition ($T_{max} < T_{adm}$) does not allow to choose the higher bed heights, which would benefit from a higher global efficiency and mass flow rate. Nevertheless, for the highest cavity height, $d = 240$ mm, the maximum temperature is less than the admissible temperature for all the nine bed heights, which allows to choose the value of b that conducts to the highest global efficiency ($b = 85$ mm). Note that as increasing the cavity height leads to a reduction of the maximum temperature, the range of bed heights that fulfil the temperature criterion increases for $d = 240$ mm. Consequently, by decreasing the maximum temperature, the highest cavity height allows to choose a bed height for which the global efficiency is significantly higher.

Those results further reinforce the advantage of choosing a cavity with a higher value of d. In particular, an increase of about 15% in the global efficiency is obtained when selecting $d = 240$ mm when compared to the other cavity heights. As such, this combination (marked with bolt in Table 4) should be selected from the ones studied in this work.

To conclude this sub-section, note that the configuration that leads to the highest global efficiency is not the same that produces the highest heating uniformity (i.e., the minimum standard deviation for the heat source distribution — see Fig. 7e). The highest heating uniformity is obtained for $b = 45$ mm and $d = 240$ mm. Nevertheless, in this study, the authors assumed that the global efficiency has priority to the heating uniformity as the main aim is to minimize the specific energy consumption of the process. Moreover, for $b = 85$ mm, the increase in the standard deviation for the heat source is only about 40% when compared to the minimum value for the heating uniformity KPI, $\sigma(\dot{Q}'''_{EM})$. As such, $b = 85$ mm and $d = 240$ mm should be the selected configuration.

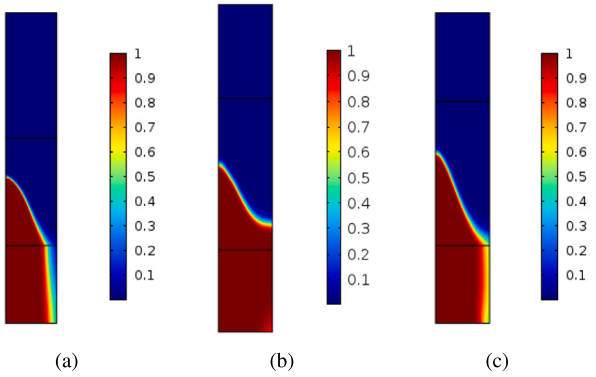

Fig. 12. Distribution of the conversion degree (α) for several geometries: (a) $b = 85$ mm and $d = 180$ mm; (b) $b = 85$ mm; $d = 240$ mm; (c) $b = 90$ mm; $d = 240$ mm.

4.1.4. Total conversion requisite

As it was mentioned in the previous sub-sections, the global efficiency increases with the bed height. As such, it would be beneficial to test values for the bed height higher than 85 mm. Nevertheless, as the heating becomes more superficial with increasing b, the regions of the bed far from the electromagnetic port will have a lower temperature. Consequently, the local temperature may not reach the reaction temperature and the total conversion will not occur if the bed height is too high.

Fig. 12 shows the distribution of the conversion degree (α) for several geometries. As the figure demonstrates, for $b = 85$ mm, the total conversion only occurred for $d = 240$ mm, which is another advantage of choosing the highest value of d. As mentioned earlier, for $d = 240$ mm the heating is more volumetric and the bed is more permeable to the electric field, which justifies the higher maximum b for which the total conversion occurred, when compared to the other cavity heights. This is also the reason why $d = 240$ mm is the only cavity height for which there is data for $b = 85$ mm in the previous sub-sections.

Fig. 12 also shows that, despite the higher heating uniformity obtained for $d = 240$ mm, if the value of b is increased to $b = 90$ mm, the total conversion is no longer verified, proving that $b = 85$ mm is the upper limit for the bed height if the total conversion is to be attained. As such, the total conversion requisite is implicitly included in the optimization domain for the values of b in Eq. (25) and is verified for all combinations studied in the previous subsections.

4.1.5. Response surface methodology (RSM)

The data presented in Fig. 7 may be interpolated to generate a continuum evolution (i.e. the response surface) of the studied variables in the domain of the optimization problem (defined in Eq. (25)). This procedure would allow to estimate the value of those variables between the data points that were simulated without the need of performing more simulations.

The interpolation was carried out using cubic splines as this technique produces a smooth behaviour between the data points, both when the solution varies significantly and when the solution assumes a more constant evolution [52]. The results were obtained with *MATLAB R2021* and are presented in Fig. 13, which shows the obtained response surfaces for the global, electromagnetic and thermal efficiencies as well as for the maximum temperature.

The conclusions that were achieved in the previous sub-sections may also be reached with the contour plots, which could be used in the design and optimization of the microwave cavity, as it was done before. For example, it is very clear from Fig. 13a that the global efficiency varies more significantly with the cavity height (d) for higher bed heights (b) than for the lower values of b. From the same figure, it is also possible to see that $b = 85$ mm and $d = 240$ mm is the optimum configuration as all admissible directions are descent directions, i.e., lead to a design configuration with lower global efficiency.

To test the error associated to the interpolation procedure without simulating any other combinations, one way is to apply the method after eliminating one of the data points of the data sample. The interpolated surface obtained without considering that point is then used to predict the interpolated variables in the eliminated point. This procedure may be repeated to every point of the sample, which may also help to conclude which points are more relevant to the interpolation technique.

Repeating this procedure to all the four variables studied in this subsection, one obtains the contour plots presented in Fig. 14, which shows the distribution of the interpolation relative error within the domain of the optimization problem. The relative error is calculated through Eq. (26).

$$e_r = \frac{|\phi_{int} - \phi_{sim}|}{\phi_{sim}} \tag{26}$$

where e_r is the relative error, ϕ_{int} is the value of the variable obtained with the interpolated surface and ϕ_{sim} is the value of the same variable obtained with the numerical simulation.

As can be seen in this figure, the errors are relatively low, specially in the interior region of the domain. As the maximum error is mainly located on the boundary of the domain, the exterior points are significantly important to increase the reliability of the interpolation. Also note that the corners cannot be removed as the error would be infinite because an extrapolation would occur. This is the reason why the corners are not represented in these graphs.

The maximum relative error is obtained for the global efficiency, being about 12.85%. As such, it is possible to conclude that this interpolation technique allows the determination of the system response with relatively high accuracy, specially in the interior region of the domain. This fact combined with the avoidance of extra numerical simulations is the main advantage of using an interpolation technique to extract a response surface from a finite data set.

4.2. 3D results — rotary kiln

Regarding the results obtained in the tridimensional case, Fig. 15 shows the influence of the axial bed velocity and the tube radius on the global, electromagnetic and thermal efficiencies. The input power and the maximum temperature are also shown. Fig. 16 shows the penetration depth distribution for different geometries used in this study; Fig. 17 shows the heat source distribution for the same geometries. Recall that these results were obtained for the tridimensional geometry depicted in Fig. 3.

4.2.1. Electromagnetic, thermal and global efficiencies

The axial bed velocity has a major influence on the efficiencies obtained in the tridimensional study. When increasing the bed velocity, there are two opposite effects on the electromagnetic efficiency: first, increasing the bed velocity makes the maximum temperature to increase (see Fig. 15e), which in turn makes the loss tangent to increase, leading to lower penetration depths and thus lower electromagnetic efficiencies; second, increasing the bed velocity makes the convective flux to increase, which pushes the reaction zone – where the temperature is higher and the penetration depth is lower – downstream of the tube, because of the reduction in the residence time. This effect may be beneficial to the electromagnetic efficiency as a high penetration depth area occurs when the velocity is higher, increasing the power dissipation in the bed.

The second effect described may be seen in Fig. 16: comparing images (a) to (b) and (c) to (d), it is quite clear that the area where the penetration depth varies the most is becoming nearer to the outlet of the reaction zone as the velocity increases. This makes a high

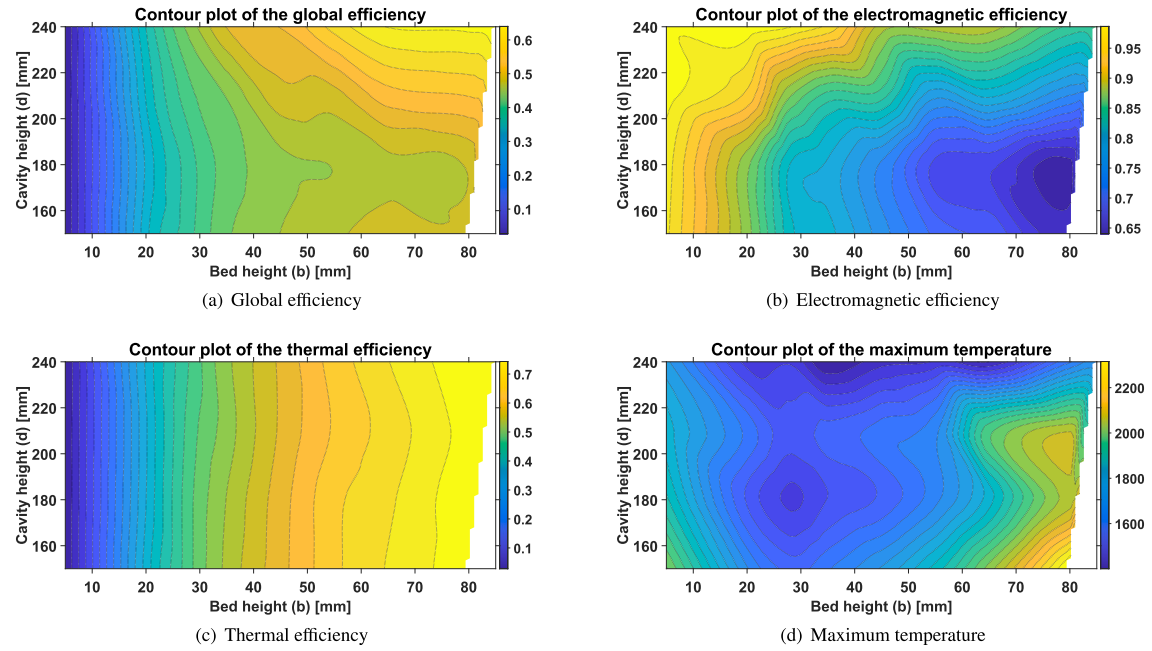

(a) Global efficiency (b) Electromagnetic efficiency

(c) Thermal efficiency (d) Maximum temperature

Fig. 13. Response surfaces obtained through the interpolation of the data presented in Fig. 7.

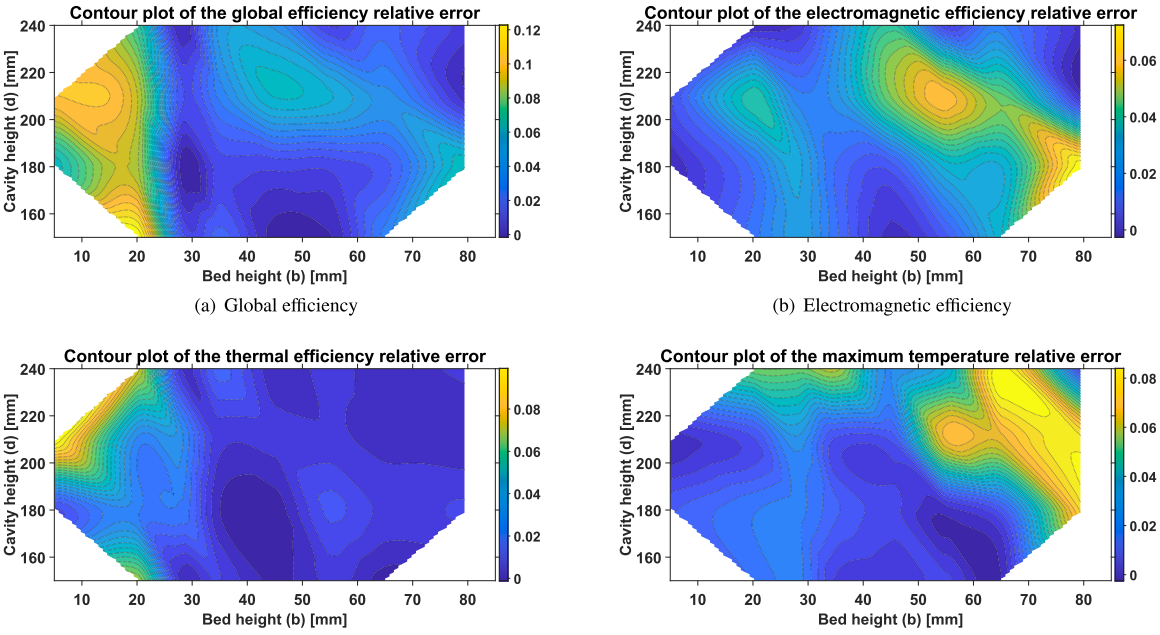

(a) Global efficiency (b) Electromagnetic efficiency

(c) Thermal efficiency (d) Maximum temperature

Fig. 14. Distribution of the relative error within the domain of the optimization problem.

penetration depth zone to appear inside the reaction zone, which in turn benefits the electromagnetic efficiency: higher penetration depths make the bed more permeable to the electric field, increasing the absorbed power for the same input power (i.e., the power delivered by the electromagnetic port). Consequently, these zones cause the electromagnetic efficiency to increase.

Although the convective flux effect is quite clear for both radii in Fig. 16, it is also clear that, for the higher radius, the high penetration depth zone is wider than for the lower radius (compare images (b) and (d) in Fig. 16). Increasing the radius leads to an increase in the surface area of the tube that is being subjected to the electromagnetic field. Consequently, for the higher radius, the electric field is more distributed within the bed region surface, making the temperature to increase nearer the outlet of the reaction zone. This effect superimposes with the effect of increasing the convective flux, making the high penetration depth area even wider. This is why this area expands more for the higher radius than for the lower one.

The effect of increasing the radius on the expansion of the high penetration depth area is clearly dominant when compared to the increase in the velocity magnitude. This is also why the expansion of this area is more prominent for the higher radius than for the lower one.

Having this into account, for the lower radius, the expansion of the high penetration depth zone is quite subtle because the surface area is lower. Thus, the electromagnetic efficiency dependency is more affected by the maximum temperature evolution. As such, the highest

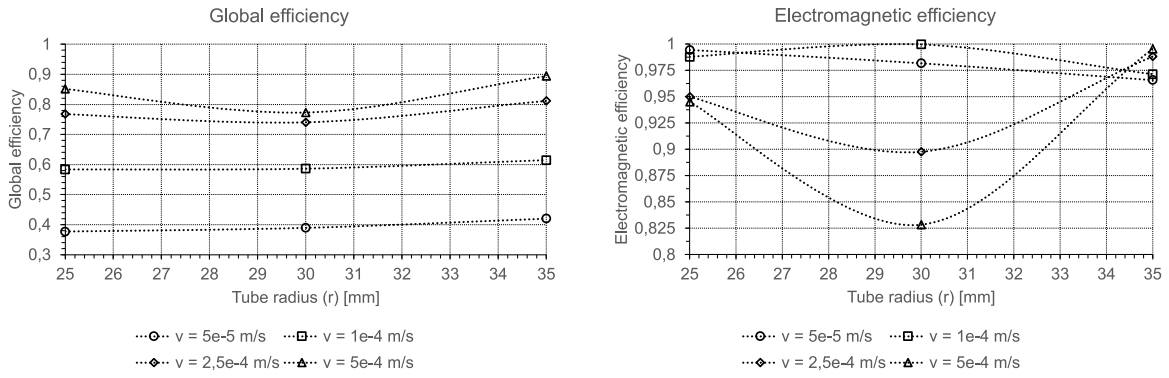

(a) Global efficiency

(b) Electromagnetic efficiency

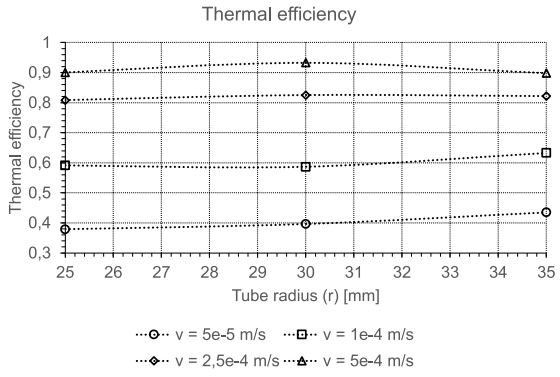

(c) Thermal efficiency

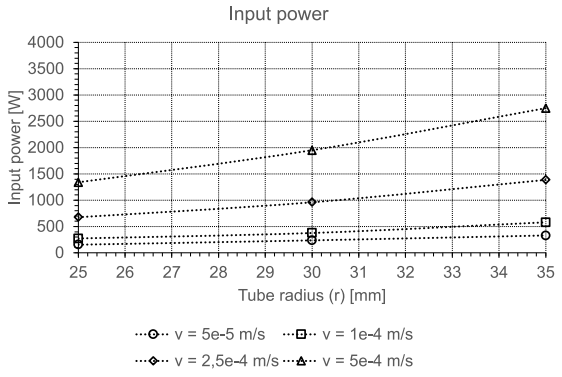

(d) Input power

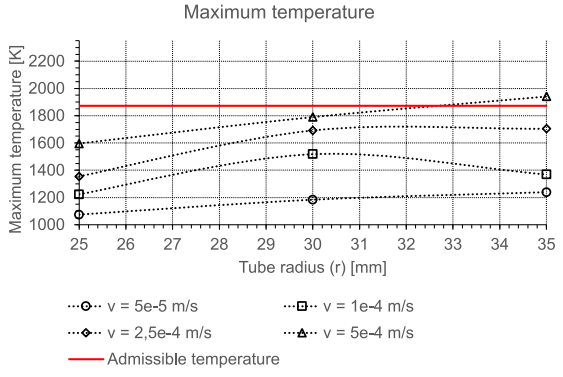

(e) Maximum temperature

Fig. 15. Results obtained for the tridimensional case, namely the dependence of several variables on the tube radius (r) and the axial bed velocity (v).

velocities lead to lower electromagnetic efficiencies (Fig. 15b) as they are associated with higher maximum temperatures (Fig. 15e).

For the higher radius, although the maximum temperature still increases with the axial velocity, the electromagnetic efficiency dependency is dominated by the appearance of the high penetration depth zone. For this radius, this zone becomes even wider when the velocity is increased. As such, the electromagnetic efficiency increases with the axial velocity (Fig. 15b).

Fig. 18 shows the evolution of the absorbed power and the thermal losses with the axial bed velocity and the tube radius. It is quite clear that increasing the bed velocity increases significantly the absorbed power within the bed material. Comparing both images (a) and (b) for a given radii, it is possible to conclude that the increase in the absorbed power is much more significant than the increase in the thermal losses. Consequently, the thermal efficiency increases with the bed velocity (Fig. 15c).

Regarding the influence of the tube radius on the thermal efficiency, Table 5 shows the evolution of the area/volume ratio with the tube radius. As expected, the area/volume ratio decreases with the tube radius. In the 3D simulations, the thermal losses are surface phenomena and the heat generation is a volumetric process. As such, it would be expected the thermal efficiency to increase with increasing the tube radius. Nevertheless, the maximum temperature also increases with the tube radius, which would cause the opposite effect: the thermal efficiency to decrease for higher radii. The combined result of these two effects is that the thermal efficiency does not vary significantly with the tube radius (Fig. 15c), as two contradictory effects are coexisting in the simulations.

The global efficiency will be affected by the physical effects described for both the electromagnetic and the thermal interfaces. It is clear from Fig. 15a that the axial bed velocity has a more significant effect on the global efficiency than the tube radius. However, for

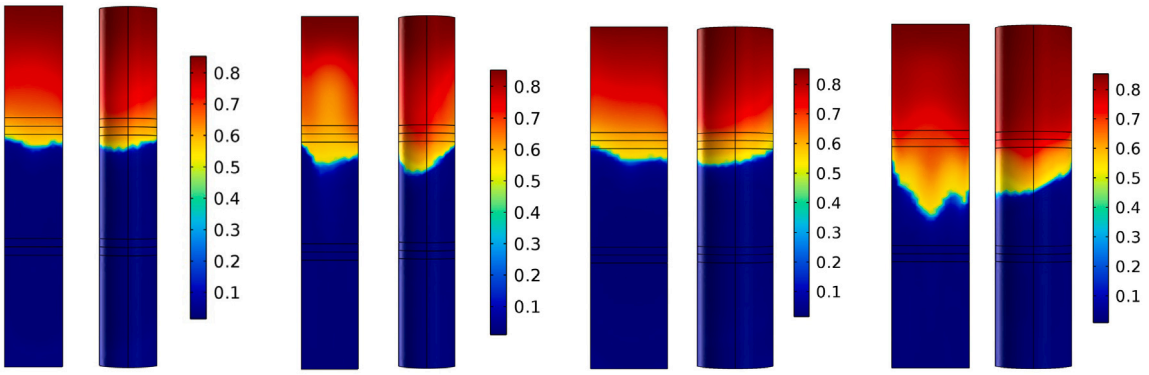

(a) $r = 25\,mm$; $v = 5 \times 10^{-5} m/s$ (b) $r = 25\,mm$; $v = 5 \times 10^{-4} m/s$ (c) $r = 35\,mm$; $v = 5 \times 10^{-5} m/s$ (d) $r = 35\,mm$; $v = 5 \times 10^{-4} m/s$

Fig. 16. Penetration depth distribution [m] for different configurations used in the 3D study: top (left image) and bottom (right image) of the bed.

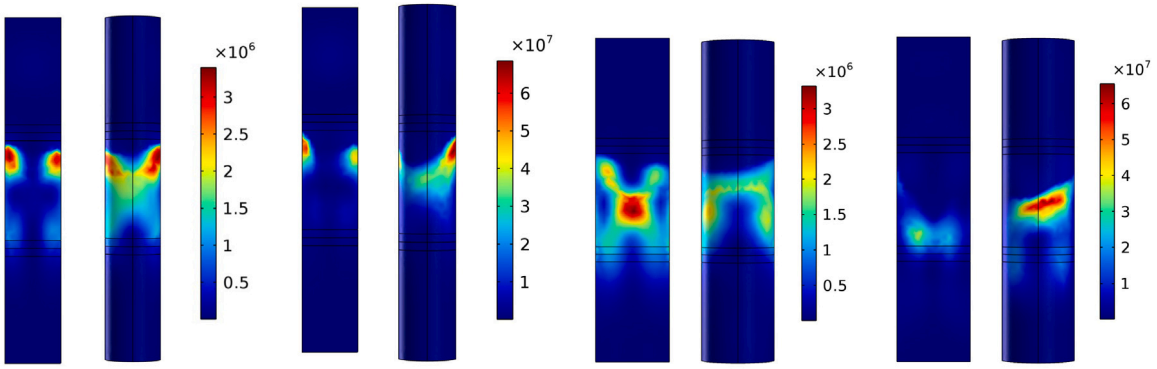

(a) $r = 25\,mm$; $v = 5 \times 10^{-5} m/s$ (b) $r = 25\,mm$; $v = 5 \times 10^{-4} m/s$ (c) $r = 35\,mm$; $v = 5 \times 10^{-5} m/s$ (d) $r = 35\,mm$; $v = 5 \times 10^{-4} m/s$

Fig. 17. Heat source distribution [W/m^3] for different configurations used in the 3D study: top (left image) and bottom (right image) of the bed.

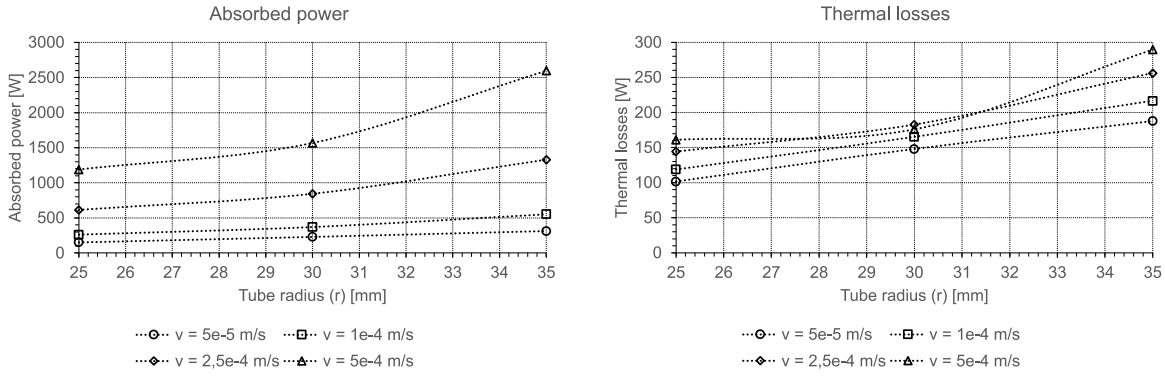

(a) Absorbed power (b) Thermal losses

Fig. 18. Evolution of the absorbed power and the thermal losses with the axial bed velocity and the tube radius.

Table 5
Dependency of the ratio area/volume on the tube radius.

Radius [mm]	Ratio area/volume
25	1617.0
30	1133.2
30	839.9

the two highest velocities, the differences in the global efficiency are reduced when compared to the two lowest values. These results also show that a proper choose for the axial solids velocity may more than double the global efficiency, reducing the operational costs and the carbon footprint in the pigment sector.

4.2.2. Maximum temperature and input power

As stated previously, the input power is implicitly computed using Eq. (19) to impose stationary regime and total conversion. The input power increases significantly with the axial velocity (Fig. 15d) due to the convective term B_1 used in Eq. (19). Moreover, the input power also increases with the tube radius (Fig. 15d) as the volume integration is increasing in the calculation of the term B_1 and the thermal losses (given by $B_{2a} + B_{2b}$) also increase with the tube radius (Fig. 18b).

Table 6
Results obtained for the constrained optimization problem defined by Eq. (25).

Radius [mm]	Velocity [m/s]	η_G [%]
25	**5×10^{-4}**	**85.1**
30	5×10^{-4}	77.3

Table 7
Summary of the key performance indicators (KPI) obtained in this work and comparison with the results available in the Literature.

KPI	Present work	Ref. [39]
η_G [%]	85.1	53.8
C_e [MJ/kg]	1.22	1.54
$\dot{m}$ [kg/h]	4.66	2.26

Regarding the maximum temperature (Fig. 15e), the evolution is quite similar to that of the input power: both variables increase with increasing the velocity and the tube radius. The reason for the maximum temperature to increase with the input power is related to the absence of mixing in the bed region. The velocity field is purely axial, which means that no transverse movement is occurring inside the reaction zone. As such, when the material enters the reaction zone and is heated up, only the axial component of the position vector is changing and the distance of the material to the electromagnetic port is practically unchanged. Consequently, the bed particles that enter the reaction zone in the area where the heat source is higher (see Fig. 17) will remain there, causing the maximum temperature to increase abruptly.

Moreover, the total conversion requisite is also responsible for the higher maximum temperatures obtained: to guarantee the total conversion, the controller increases the average temperature of the bed, which makes the maximum temperature to increase abruptly when no mixing is occurring.

Increasing the velocity or the tube radius is not a good strategy to reduce the maximum temperature, contrary to what happened in the bidimensional case, where increasing the cavity heigh d helped to reduce the maximum temperature. However, significant increases in the global efficiency may be obtained by increasing the velocity magnitude.

4.2.3. Constrained optimization

Following the same procedure used in the bidimensional study, the optimization problem defined by Eq. (25) was re-solved for the tridimensional data set. The optimization domain is now defined as follows: $v \in [5 \times 10^{-5}, 5 \times 10^{-4}]$ m/s $\wedge$ $r \in [25, 35]$ mm.

By inspecting Fig. 15a, it is possible to see that the global efficiency is higher for $v = 5 \times 10^{-4}$ m/s for all the radii studied. At the same time, Fig. 15e shows that for $v = 5 \times 10^{-4}$ m/s and $r = 35$ mm, the maximum temperature exceeds the thermal limit prescribed in this work (given by the red line in the same figure). Consequently, that point must be excluded as it does not fulfil the temperature criterion.

From these observations, it is possible to conclude that the maximum global efficiency will be given by one of the two points that remain for $v = 5 \times 10^{-4}$ m/s. These two points are shown in Table 6 with the associated global efficiencies.

From Table 6, it is possible to choose the configuration that produces the highest global efficiency, marked with bolt in the table: $r = 25$ mm and $v = 5 \times 10^{-4}$ m/s. In this case, the lower radius is the best configuration, to benefit from a higher electromagnetic efficiency.

4.2.4. Specific energy consumption and yield

Table 7 shows the main key performance indicators (KPI) obtained for the best configuration (which was chosen in the previous section). The specific energy consumption (C_e) and the yield ($\dot{m}$) are included in this table and a comparison with the previous work done by the authors [39], where a different microwave cavity was used, is made.

Table 8
Results obtained for the parametric study regarding the input power for $r = 20$ mm and $v = 5 \times 10^{-4}$ m/s.

Variable	Value
$P_{port,min}$ [W]	1100
η_G [%]	65.4
η_{EM} [%]	88.3
η_T [%]	74.1
C_e [MJ/kg]	1.33

The results show that the present configuration allows an increase in the global efficiency close to 30%, while the specific energy consumption decreases about 21%. The yield increases through a factor of 2, which means that this new configuration is more attractive for all the variables used as KPI.

The reasons for this improvement are related to the opening of the cavity and the use of thermal insulation in the areas where the temperature is higher. The thermal efficiency is the main driver for this improvement as it increases from 54.0% to 90.1%, due to a significant reduction in the thermal losses of the system.

4.2.5. The constant power case

As the controller uses Eq. (19) to compute the input power, it imposes automatically the stationary regime ($\partial/\partial t = 0$) and total conversion ($\alpha = 0.999$ at the outlet of the reactor). This ensures that the power that is delivered to the system is the minimum required to process all the material inside the reactor.

Nevertheless, for the cases with low thermal efficiency, as for the configurations with lower radii or lower velocities, Eq. (19) may underestimate the input power and the total conversion may not occur at all, which happened for $r = 20$ mm, the lowest radius studied in this work. As such, the authors decided to perform a parametric study on the input power to access the minimum power necessary to process the material.

The results are shown in Table 8. The minimum input power for which all material reacted is shown in the table, which is around 1100 W. If the input power is increased above this value, the total conversion requisite will still occur but the input power will not be at its minimum. Consequently, the specific energy consumption will not be minimized. Moreover, if the input power is reduced below 1100 W, the material will not react completely.

The results also show that this configuration is less efficient than the one obtained in Section 4.2.3 as the optimal configuration: the global efficiency is only 65.4% and the specific energy consumption is about 0.11 MJ/kg higher than the value obtained for $r = 25$ mm and $v = 5 \times 10^{-4}$ m/s. These results were expected as a lower radius is being used, which jeopardizes the thermal efficiency (about 16% lower than the optimal case).

4.3. Potential of microwave technology to decarbonize the sector

The future carbon footprint associated to the microwave production may be estimated knowing that electricity is the energy source for microwave devices. The electricity conversion factors allow to estimate the green-house gas (GHG) emissions in the production phase of the pigment. This may be done using Eq. (27), which uses the specific energy consumption estimated earlier in this work:

$$E_{CO_{2,eq}} = f_{GHG}\, C_e \tag{27}$$

where $E_{CO_{2,eq}}$ is the estimated specific GHG emissions to produce 1 kg of pigment [$kg_{CO_{2,eq}}/kg_{pigment}$], f_{GHG} is the conversion factor from electricity [$kg_{CO_{2,eq}}$/MJ] and C_e is the specific energy consumption [$MJ/kg_{pigment}$].

The conversion factors will depend on the energy mix available in each country or region, particularly on the renewable electricity share

Table 9
Results obtained for the GHG specific emissions.

Country	f_{GHG} [$kg_{CO_{2,eq}}$/kWh]	$E_{CO_{2,eq}}$ [$kg_{CO_{2,eq}}/kg_{pigment}$]
Germany	0.33866	0.115
USA (Maine)	0.1035	0.0351
Sweden	0.00567	0.00192

present on the energy mix. The conversion factors for different regions are shown in Table 9, for comparison. The specific energy consumption will be set to $C_e = 1.22$ MJ/$kg_{pigment}$ = 0.339 kWh/$kg_{pigment}$, as this was the value estimated by the numerical simulations combined with the optimization procedure.

Table 9 also shows the results obtained for the GHG emissions using microwave technology. Eq. (27) together with the conversion factors presented in the same table were used to calculate these values, which may be compared to the reference value for the conventional process, $E_{CO_{2,eq}} = 0.385$ $kg_{CO_{2,eq}}/kg_{pigment}$ [39].

In the regions considered, the amount of GHG emitted to the atmosphere is significantly lower using microwave technology, as the value presented in the third column in Table 9 is less than 0.385 for all regions. This is due to the use of electricity combined with high shares of renewable sources in the energy mixes available in these regions and higher efficiencies obtained for the microwave process. As such, microwave heating is a promising and successful technology to decarbonize the pigment sector.

Note that these calculations only consider the energy used to produce the pigment (i.e. electricity in microwave heating vs natural gas in the conventional process). The energy used in other stages of the process (raw material preparation, transport, storage, etc.) was not considered as those processes are out of the scope of this work.

Now that the specific GHG emissions are estimated, it is possible to estimate the cumulative GHG emissions in this sector through the years. This is specially useful to predict when the carbon neutrality will be achieved in the pigment sector. To estimate the cumulative emissions, the following assumptions were made:

- The total worldwide production in the pigment sector was 6 million tonnes in 2024 (the same value as in 2005 [53]); this value will be assumed to increase at a constant rate of 0.5% per year, which will allow to estimate the pigment production in the upcoming years;
- Two scenarios were considered: scenario 1, where no transition for microwave technology occurs and the production will continue through the conventional process; and scenario 2, where microwave technology will substitute the conventional process — initially only partly and afterwards fully;
- In scenario 2, at first the total production is shared by the conventional process and the microwave technology. The fraction of pigments produced by microwave devices will be defined as s. In the first 4 years, we assumed that microwave technology will not participate in the production for industry adaption ($s = 0$). Afterwards, the microwave technology share will increase at a constant rate ds — the microwave growth rate. Several values for ds were considered (3, 5, 7 and 10% per year).
- Following the procedure presented earlier, the specific GHG emissions associated to the fraction that is produced by microwave technology will be calculated using Eq. (27). For the conventional process, an average value of $E_{CO_{2,eq}} = 0.385$ $kg_{CO_{2,eq}}/kg_{pigment}$ was used [39];
- In this analysis, we will assume that this pigment is representative of all the pigment production worldwide, as there is no data for all the pigments produced in the world. Hence, the value $C_e = 1.22$ MJ/$kg_{pigment}$ will be assumed to be valid for the total pigment production in the world;
- To implement a conservative approach, the specific energy consumption (C_e) and the conversion factors from electricity (f_{GHG}) will be assumed to be constant during the next decades. This will ignore any improvements in the energy efficiency of microwave devices and any increases in the share of renewable energy sources — although both changes are likely to occur.

For each year, the total production capacity is estimated and the fraction of microwave technology is then computed. Knowing the amount of pigments that is produced through the conventional process and using microwave technology, then it is possible to calculate the GHG emissions in that year by applying the procedure already described. The cumulative emissions are then calculated by summing up all the emissions from the past years.

The results are shown in Fig. 19. Fig. 19a shows the influence of the microwave growth rate (ds) on the fraction of pigments produced by microwave technology and by the conventional process. It is evident that for microwave growth rates lesser than 5% the conventional process will still be used in 2050. As such, to fulfil the goals established by the Intergovernmental Panel on Climate Change (i.e., a null emission balance in 2050), a minimum value of $ds = 5\%$ must be implemented.

These same conclusions may also be achieved through Fig. 19b: note that for $ds = 5\%$, the carbon neutrality in the process stage will be achieved in 2046, while for $ds = 10\%$ the emissions will stabilize 10 years earlier, in 2036. For the $ds = 3\%$, the emissions will not stabilize in 2050.

Note that the null emission balance is represented in this graph by a practically horizontal line in the cumulative emissions (meaning that the emissions will not increase significantly as the conversion factor is very low in Sweden). Nevertheless, during the transition, for the best case scenario ($ds = 10\%$), the calculations predict that more than 20 million tonnes of GHG will be emitted to the atmosphere, which further reinforces the urgency to implement microwave technology.

Fig. 19c shows the influence of the conversion factor in the cumulative emissions for an intermediate value of the microwave growth rate ($ds = 7\%$). These results clearly show that, even if microwave technology has a share of 100% in the pigment sector, the emissions will continue to increase if the electricity is produced from fossil fuels. Note that the countries where the conversion factor (f_{GHG}, see Table 9) for electricity is higher (the case of Germany) exhibit a higher slope in the cumulative emissions in 2050. On the other hand, in the countries where the renewable sources are more developed (the case of Sweden), the cumulative emissions will practically stabilize as soon as microwave technology achieves a 100% share in the pigment sector.

Finally, despite the simple calculations employed in this section, these results clearly show that to implement a real decarbonization strategy, microwave technology will have to participate further in the pigment production and the renewable sources of electricity will have to be developed in some countries. This emission projection will also be useful to the decision makers in the development of energy policies that may contribute to achieve the goals for the industry decarbonization.

5. Concluding remarks

As part of the decarbonization goals, microwave technology has been emerging as a promising way to reduce the GHG emissions in the industry sector. This work addresses the high temperature processing of the Brown 24 ceramic pigment through a detailed numerical study. The mathematical model includes the coupling between the chemical, thermal and electromagnetic interfaces and a moving plunger was used to impose the impedance matching in the cavity, maximizing the electromagnetic efficiency. The plunger position was automatically managed by a controller developed in *MATLAB* and adapted from previous works.

The influence of several design variables was addressed, which allowed to choose the best configuration from the ones studied in this

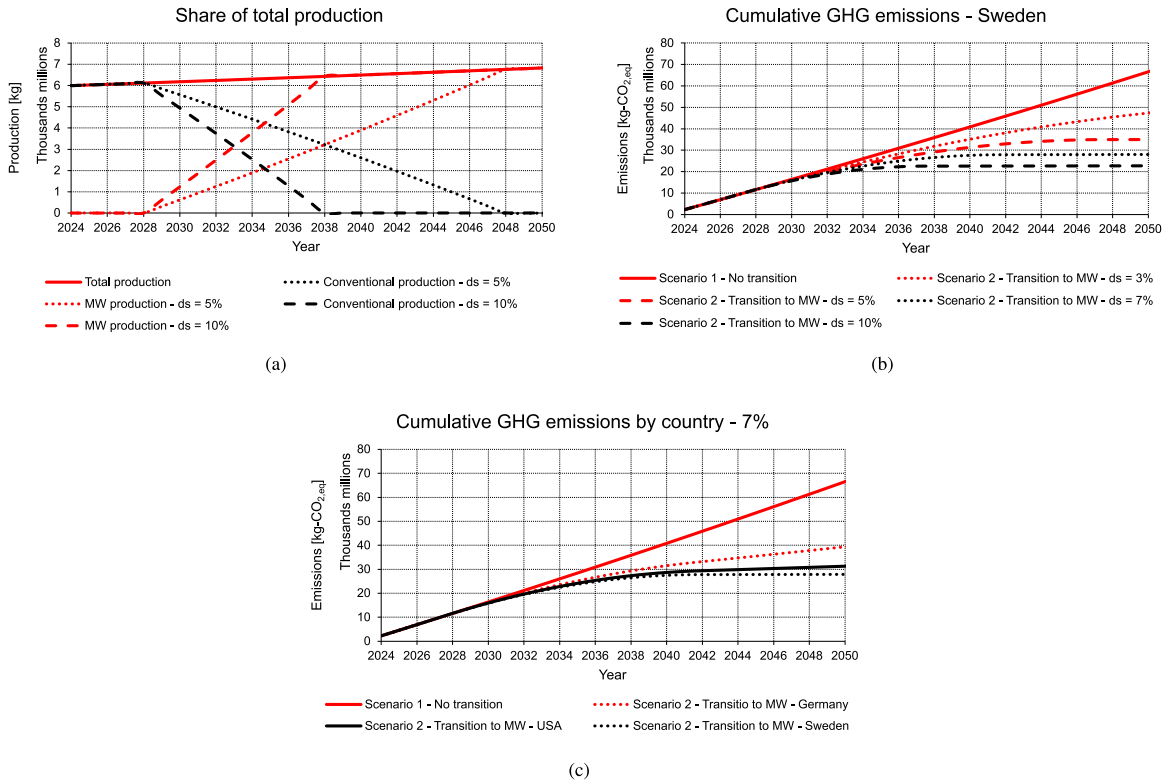

Fig. 19. Results obtained for the emissions analysis: (a) share of conventional and microwave technologies on the total production for different microwave growth rates (ds); (b) cumulative GHG emissions in Sweden for different microwave growth rates; (c) cumulative GHG emissions in different countries/regions for a microwave growth rate of $ds = 7\%$.

work. The design variables include the cavity height (d) and the bed height (b) in the bidimensional study and the axial solids velocity (v) and the tube radius (r) in the tridimensional one. The optimization was based on several key performance indicators (KPI), namely the global, electromagnetic and thermal efficiencies, the yield, the specific energy consumption and the heat source standard deviation.

The main conclusions achieved in the bidimensional study are addressed as follow:

(i) The cavity height (d) has a major effect on the global efficiency of the process, particularly on the electromagnetic interface. As the cavity height increases, a low temperature region in the inlet of the reaction zone becomes wider. That region is highly permeable to the electric field due to higher local penetration depths, which increase the electric field norm inside the load and, consequently, the absorbed power. As such, increasing the cavity height leads to an increase in the electromagnetic efficiency up to 20%. Moreover, as the cavity height increases, the maximum temperature and the heat source standard deviation reduce, which is another advantage of this geometry. This may be specially beneficial for the heating of high loss tangent materials that undergo chemical reactions, as the heating heterogeneity may lead to lower local temperatures and thus to an incomplete conversion of reactants into products. Additionally, reducing the maximum temperature decreases the risk of melting the load;

(ii) The electromagnetic efficiency decreases significantly with the bed height (b), due to the attenuation phenomenon that occurs. This is caused as the characteristic length of the bed (in this case, b) is much higher than the local penetration depth, leading to a superficial heating that penalizes the electromagnetic efficiency. Nevertheless, the global efficiency increases with b as the thermal efficiency increases significantly for the higher bed heights;

(iii) The configuration that produces the highest global efficiency is $b = 85$ mm and $d = 240$ mm with $\eta_G = 66.4\%$. By increasing the cavity height (d), the reduction in the maximum temperature allowed to choose a bed height for which the global efficiency is higher, while for the lower cavity heights the configurations with higher global efficiency had to be rejected for not fulfilling the temperature criterion ($T < T_{adm}$). This aspect is another advantage of increasing the value of d;

(iv) The maximum bed height for which the total conversion requisite is fulfilled is $b = 85$ mm for $d = 240$ mm and $b = 80$ mm for the remaining values of d. As such, increasing the cavity height proved to be a successful way of increasing the maximum bed heigh for which the total conversion occurs;

(v) The obtained numerical data may be interpolated with high accuracy to produce smooth response surfaces that may be used in the design of microwave cavities. Moreover, the response surfaces may help to predict the behaviour of a configuration that has not been simulated, avoiding extra numerical simulations, with error below 12%.

Regarding the tridimensional study, the main conclusions are:

(i) The global efficiency is highly affected by the axial solids velocity. In particular, differences up to 45% in the global efficiency may be obtained between the lowest and the highest velocities tested in this work. Increasing the tube radius or the axial velocity is not a suitable strategy to decrease the maximum temperature due to the absence of mixing in the bed region;

(ii) The configuration that leads to the highest global efficiency is $v = 5 \times 10^{-4}$ m/s and $r = 25$ mm, for which $\eta_G = 85.1\%$, $C_e = 1.22$ MJ/kg and $\dot{m} = 4.66$ kg/h. Significant improvements for these variables were obtained when compared to the microwave cavity tested by the authors in previous works [39].

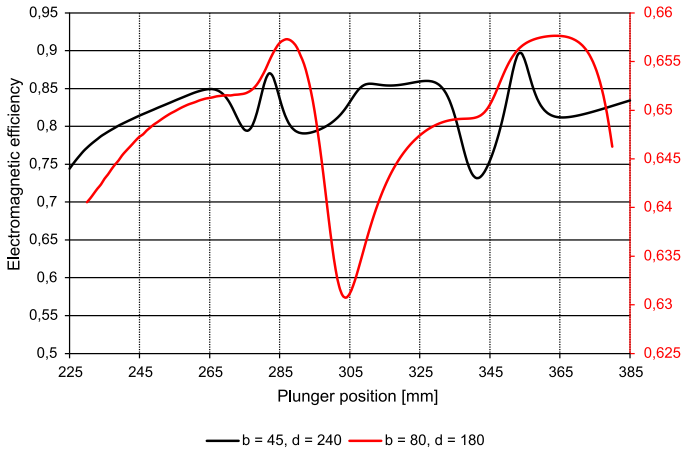

(a) Dependence of the electromagnetic efficiency on the plunger position. The values of b and d are in mm.

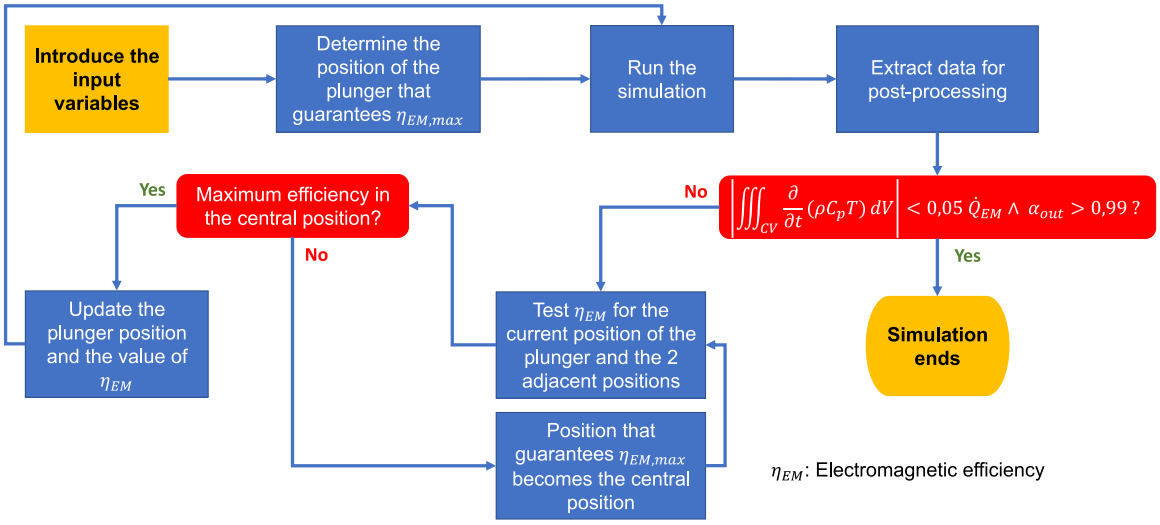

(b) Flowchart of the controller algorithm [50].

Fig. 20. Some features of the MATLAB controller. Details may be found in Section 3.

Comparing the conveyor belt and the rotary kiln configurations, one may conclude that the latter is more efficient and allows a higher mass flow rate. Moreover, in the rotary kiln, the maximum temperatures are lower, which makes this configuration more suitable for this material when compared to the conveyor belt counterpart. Nevertheless, the solids velocity inside the bed is much simpler to solve for the conveyor belt configuration and an optimization study including more design variables may lead to better results for this configuration. In particular, testing cavity heights higher than 240 mm may be of interest to see the effect in the global efficiency.

These results also show that some typical problems related to microwave heating (as the high maximum temperatures and the melting of the load) may be overpassed through a proper design of the microwave cavity — being the increase in the cavity height an example of such a situation. It is important to mention that the overall gains, obtained through optimization, for the different KPI were obtained with same MATLAB controller.

The results obtained in this work clearly demonstrate that microwave technology is a promising alternative to the conventional heating. Firstly, the higher global efficiencies related to microwave heating allow to decrease the energy consumption of the process and thus reduce the carbon footprint in the pigment sector. Secondly, the specific GHG emissions are lower when using microwave energy.

Microwave technology is a promising way of decarbonizing the pigment sector, allowing a practical null emission balance right in 2050 if electricity is produced mainly from renewable sources. The results clearly show that to achieve the decarbonization goals prescribed by the IPCC, the industry must move ahead towards a more sustainable heating mechanism, which would have to occur in the next decade.

Finally, the results show the importance of an energy efficiency study in the context of a decarbonization era: reducing the energy consumption of the processes will be mandatory as it decreases the operational costs, makes new technologies more feasible in the techno-economic field and increases the chances of a process to depend exclusively on renewable energy sources.

CRediT authorship contribution statement

Pedro A.V. Ramos: Writing – original draft, Visualization, Validation, Methodology, Investigation, Formal analysis. **Duarte M.S. Albuquerque:** Supervision, Resources, Project administration, Methodology, Conceptualization. **José C.F. Pereira:** Writing – review & editing, Supervision, Funding acquisition.

Declaration of competing interest

The authors declare that they have no known competing financial interests or personal relationships that could have appeared to influence the work reported in this paper.

Data availability

Data will be made available on request.

Acknowledgements

The authors wish to thank José Luis Godes from Al-Farben for clarifying doubts concerning the chemistry of the pigments. These results are contributions from the project DESTINY, which has received funding from the European Union's Horizon 2020 research and innovation programme under grant agreement no. 820783.

The authors are also grateful to the anonymous reviewers for their insightful and constructive comments that allowed us to improve the article.

The authors acknowledge Fundação para a Ciência e a Tecnologia (FCT) for its financial support via the projects LAETA Base Funding (DOI: 10.54499/UIDB/50022/2020) and LAETA Programatic Funding (DOI: 10.54499/UIDP/50022/2020).

Pedro A.V. Ramos acknowledges Fundação para a Ciência e a Tecnologia (FCT) through Contract No. 2021.05552.BD.

Appendix. Details about the MATLAB controller

Some details regarding the controller are presented in Fig. 20, including the dependence of the electromagnetic efficiency with the plunger position and a flowchart of the controller algorithm. The details of the computational model may be found in Section 3.

References

[1] Masson-Delmotte V, Zhai P, Pirani A, Connors SL, Péan C, Berger S, et al., editors. Summary for policymakers. In: Climate change 2021: The physical science basis. Contribution of working group I to the sixth assessment report of the intergovernmental panel on climate change. IPCC; 2021, in press.

[2] Metaxas AC, Meredith RJ, editors. Industrial microwave heating. 1st ed.. The Institution of Engineering and Technology; 1983.

[3] Das S, Mukhopadhyay A, Datta S, Basu D. Prospects of microwave processing: An overview. Bull Mater Sci 2009;32(1):1–13. http://dx.doi.org/10.1007/s12034-009-0001-4.

[4] Li B, Fan X, Yu S, Xia H, Nong Y, Bian J, et al. Microwave heating of biomass waste residues for sustainable bioenergy and biomass materials preparation: A parametric simulation study. Energy 2023;274:127347. http://dx.doi.org/10.1016/j.energy.2023.127347.

[5] Siddique IJ, Salema AA, Antunes E, Vinu R. Technical challenges in scaling up the microwave technology for biomass processing. Renew Sustain Energy Rev 2022;153:111767. http://dx.doi.org/10.1016/j.rser.2021.111767.

[6] Makul N, Rattanadecho P, Agrawal DK. Applications of microwave energy in cement and concrete – A review. Renew Sustain Energy Rev 2014;37:715–33. http://dx.doi.org/10.1016/j.rser.2014.05.054.

[7] Amini A, Latifi M, Chaouki J. Electrification of materials processing via microwave irradiation: A review of mechanism and applications. Appl Therm Eng 2021;193:117003. http://dx.doi.org/10.1016/j.applthermaleng.2021.117003.

[8] Zhu J, Kuznetsov A, Sandeep K. Mathematical modeling of continuous flow microwave heating of liquids (effects of dielectric properties and design parameters). Int J Therm Sci 2007;46(4):328–41. http://dx.doi.org/10.1016/j.ijthermalsci.2006.06.005.

[9] Patil N, Rebrov E, Esveld D, Eränen K, Benaskar F, Meuldijk J, et al. Effect of the load size on the efficiency of microwave heating under stop flow and continuous flow conditions. J Microw Power Electromagn Energy 2012;46(2):83–92. http://dx.doi.org/10.1080/08327823.2012.11689827.

[10] Yousefi T, Mousavi S, Saghir M, Farahbakhsh B. An investigation on the microwave heating of flowing water: A numerical study. Int J Therm Sci 2013;71:118–27. http://dx.doi.org/10.1016/j.ijthermalsci.2013.04.006.

[11] Tuta S, Palazoğlu TK. Finite element modeling of continuous-flow microwave heating of fluid foods and experimental validation. J Food Eng 2017;192:79–92. http://dx.doi.org/10.1016/j.jfoodeng.2016.08.003.

[12] Gao X, Liu X, Yan P, Li X, Li H. Numerical analysis and optimization of the microwave inductive heating performance of water film. Int J Heat Mass Transfer 2019;139:17–30. http://dx.doi.org/10.1016/j.ijheatmasstransfer.2019.04.122.

[13] D'Ambrosio R, Cintio A, Lazzeri A, Annino G. Design of an overmoded resonant cavity-based reactor for ceramic matrix composites production. Chem Eng J 2021;405:126609. http://dx.doi.org/10.1016/j.cej.2020.126609.

[14] Guo F, Qiao Q, Mao S, Bai J, Dong K, Shu R, et al. A comprehensive study on the pyrolysis behavior of pine sawdust catalyzed by different metal ions under conventional and microwave heating conditions. Energy 2023;272:127115. http://dx.doi.org/10.1016/j.energy.2023.127115.

[15] Li F, Sun D, Zha Z, Yang K, Ge Z, Zhang H. Numerical simulation of the coupled multiphysics fields and reactions during the microwave pyrolysis of wood particles. Energy 2023;283:128493. http://dx.doi.org/10.1016/j.energy.2023.128493.

[16] Darvishi H, Khodaei J, Behroozi-Khazaei N, Salami P, Akhijahani HS. Greenhouse gas emission reduction potential, energy and exergy analysis of combined microwave-convective dryer. Energy 2023;285:128772. http://dx.doi.org/10.1016/j.energy.2023.128772.

[17] Foong SY, Liew RK, Yek PNY, Han CS, Phang XY, Chen X, et al. Microwave heating combined with activated carbon reaction bed: An energy-saving approach to convert seawater into freshwater. Energy 2023;272:127178. http://dx.doi.org/10.1016/j.energy.2023.127178.

[18] Liu J, Xue Y, Fu Y, Yao K, Liu J. Numerical investigation on microwave-thermal recovery of shale gas based on a fully coupled electromagnetic, heat transfer, and multiphase flow model. Energy 2023;263:126090. http://dx.doi.org/10.1016/j.energy.2022.126090.

[19] He J, Yang Y, Zhu H, Li K, Yao W, Huang K. Microwave heating based on two rotary waveguides to improve efficiency and uniformity by gradient descent method. Appl Therm Eng 2020;178:115594. http://dx.doi.org/10.1016/j.applthermaleng.2020.115594.

[20] Zhu H, He J, Hong T, Yang Q, Wu Y, Yang Y, et al. A rotary radiation structure for microwave heating uniformity improvement. Appl Therm Eng 2018;141:648–58. http://dx.doi.org/10.1016/j.applthermaleng.2018.05.122.

[21] Tang Z, Hong T, Liao Y, Chen F, Ye J, Zhu H, et al. Frequency-selected method to improve microwave heating performance. Appl Therm Eng 2018;131:642–8. http://dx.doi.org/10.1016/j.applthermaleng.2017.12.008.

[22] Energy efficiency 2021. International Energy Agency; 2021.

[23] Mechenova V, Yakovlev V. Efficiency optimization for systems and components in microwave power engineering. J Microw Power Electromagn Energy: Publ Int Microw Power Inst 2004;39:15–29. http://dx.doi.org/10.1080/08327823.2004.11688505.

[24] Moon E, Yakovlev V. Computer-aided design of a dielectric insert supporting uniformity of fast microwave heating. COMPEL - Int J Comput Math Electr Electron Eng 2018;37(6):1958–68. http://dx.doi.org/10.1108/COMPEL-06-2017-0266.

[25] Mäkelä M. Experimental design and response surface methodology in energy applications: A tutorial review. Energy Convers Manage 2017;151:630–40. http://dx.doi.org/10.1016/j.enconman.2017.09.021.

[26] Fan Y, Jin L, Ji W, Wang J, Zhu L, Zhao W. Microwave-induced carbonization of rapeseed shell for bio-oil and bio-char: Multi-variable optimization and microwave absorber effect. Energy Convers Manage 2019;191:23–38. http://dx.doi.org/10.1016/j.enconman.2019.04.020.

[27] Abea A, Kravets M, Gou P, Guàrdia MD, Felipe X, Bañón S, et al. Modeling of radio frequency heating of packed fluid foods moving on a conveyor belt: A case study for tomato puree. Innov Food Sci Emerg Technol 2023;86:103386. http://dx.doi.org/10.1016/j.ifset.2023.103386.

[28] Chen W, Shen C, Jiang Q, Ma H. Conveyor belt catalytic infrared radiation as a novel apparatus for dried tofu baking: Focus on evaluation of physicochemical qualities. Innov Food Sci Emerg Technol 2024;95:103703. http://dx.doi.org/10.1016/j.ifset.2024.103703.

[29] Alamia A, Ström H, Thunman H. Design of an integrated dryer and conveyor belt for woody biofuels. Biomass Bioenergy 2015;77:92–109. http://dx.doi.org/10.1016/j.biombioe.2015.03.022.

[30] Vermeiren J, Dilissen N, Goovaerts V, Vleugels J. Electrification of clinker and calcination treatments in the cement sector by microwave technology – A review. Constr Build Mater 2024;428:136271. http://dx.doi.org/10.1016/j.conbuildmat.2024.136271.

[31] Watkinson A, Brimacombe JK. Heat transfer in a direct-fired rotary kiln: II heat flow results and their interpretation. Metall Trans B 1978;9(3):209–19. http://dx.doi.org/10.1007/BF02653686.

[32] Tscheng SH, Watkinson AP. Convective heat transfer in a rotary kiln. Can J Chem Eng 1979;57(4):433–43. http://dx.doi.org/10.1002/cjce.5450570405.

[33] Ginsberg T, Modigell M. Dynamic modelling of a rotary kiln for calcination of titanium dioxide white pigment. Comput Chem Eng 2011;35(11):2437–46. http://dx.doi.org/10.1016/j.compchemeng.2011.03.029.

[34] Agrawal A, Ghoshdastidar P. Numerical simulation of heat transfer during production of rutile titanium dioxide in a rotary kiln. Int J Heat Mass Transfer 2017;106:263–79. http://dx.doi.org/10.1016/j.ijheatmasstransfer.2016.10.024.

[35] Dorn C, Behrend R, Giannopoulos D, Napolano L, Baños BG, James V, et al. KPI and LCA evaluation of integrated microwave technology for high temperature processes. Procedia CIRP 2015;29:492–7. http://dx.doi.org/10.1016/j.procir.2015.02.033, The 22nd CIRP Conference on Life Cycle Engineering.
[36] https://www.destinyh2020andbeyond.eu/.
[37] Alifieris O, Katsourinis D, Giannopoulos D, Founti M. Process simulation and life cycle assessment of ceramic pigment production: A case study of green Cr2O3. Processes 2021;9:1731. http://dx.doi.org/10.3390/pr9101731.
[38] Gonçalves SN, Albuquerque DM, Pereira JC. Modelling and energy efficiency analysis of the microwave continuous processing of limestone. J Clean Prod 2024;142912. http://dx.doi.org/10.1016/j.jclepro.2024.142912.
[39] Ramos PA, Albuquerque DM, Pereira JC. Numerical simulation and optimization of the ceramic pigments production process using microwave heating. Chem Eng Process - Process Intensif 2021;169:108567. http://dx.doi.org/10.1016/j.cep.2021.108567.
[40] Electromagnetic characterization of raw materials. DESTINY Project Consortium; 2019, Deliverable published by the DESTINY Project. Grant Agreement: 820783. Available online at https://cordis.europa.eu/project/id/820783/results.
[41] Chemical reaction engineering module user's guide. COMSOL AB; 2015, Version 5.1.
[42] Heat transfer module user's guide. COMSOL AB; 2015, Version 5.1.
[43] RF module user's guide. COMSOL AB; 2015, Version 5.1.
[44] Pozar DM. Microwave engineering. 4th ed.. John Wiley & Sons; 2011.
[45] Song C-W, Lee S-Y. Design of a solenoid actuator with a magnetic plunger for miniaturized segment robots. Appl Sci 2015;5(3):595–607. http://dx.doi.org/10.3390/app5030595.
[46] Valverde C, Rodríguez-García M-M, Rojas E, Bayón R. State of the art of the fundamental aspects in the concept of microwave-assisted heating systems. Int Commun Heat Mass Transfer 2024;156:107594. http://dx.doi.org/10.1016/j.icheatmasstransfer.2024.107594.
[47] García-Baños B, Catala-Civera J, Penaranda-Foix F, Plaza-Gonzalez P, Llorens G. In situ monitoring of microwave processing of materials at high temperatures through dielectric properties measurement. Materials 2016;9:349. http://dx.doi.org/10.3390/ma9050349.
[48] Gale W, Totemeir T, editors. Smithells metals reference book. 8th ed.. Elsevier; 2004.
[49] https://www.rath-group.com/en, Visited on 16th April 2021.
[50] Mimoso RM, Albuquerque DM, Pereira JM, Pereira JC. Simulation and control of continuous glass melting by microwave heating in a single-mode cavity with energy efficiency optimization. Int J Therm Sci 2017;111:175–87. http://dx.doi.org/10.1016/j.ijthermalsci.2016.08.015.
[51] Mendes J. Simulation of cement clinker process by of microwave heating. Instituto Superior Técnico; 2017.
[52] Gülüm M, Yesilyurt MK, Bilgin A. The performance assessment of cubic spline interpolation and response surface methodology in the mathematical modeling to optimize biodiesel production from waste cooking oil. Fuel 2019;255:115778. http://dx.doi.org/10.1016/j.fuel.2019.115778.
[53] Faulkner EB, Schwartz RJ, editors. High performance pigments. 2nd ed.. Wiley-VCH; 2009.